



FCTUC FACULDADE DE CIÊNCIAS
E TECNOLOGIA
UNIVERSIDADE DE COIMBRA

RUI MIGUEL PARENTE ABREU

AUTOMATIC LOCATION OF ATHEROSCLEROTIC PLAQUES BY ULTRASOUNDS

*Dissertation presented to the Faculty of Sciences and Technology
of the University of Coimbra
to obtain a Master's degree in Biomedical Engineering*

SUPERVISORS:

JAIME BATISTA DOS SANTOS (DEEC-UC)

JOSÉ SILVESTRE SILVA (DCTE-AM)

MARIA ALEXANDRA DE ALBUQUERQUE ANDRÉ (ESTESC-IPC)

COIMBRA, 2016

THIS WORK WAS DEVELOPED IN COLLABORATION WITH:

FACULDADE DE CIÊNCIAS TECNOLOGIA

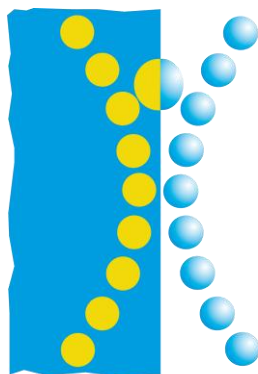
UNIVERSIDADE DE COIMBRA



• U • C •

FCTUC FACULDADE DE CIÊNCIAS
E TECNOLOGIA
UNIVERSIDADE DE COIMBRA

ESCOLA SUPERIOR DE TECNOLOGIA DA SAÚDE COIMBRA



ESCOLA
SUPERIOR DE
TECNOLOGIA DA
SAÚDE DE
COIMBRA

Esta cópia da tese é fornecida na condição de que quem a consulta reconhece que os direitos de autor são pertença do autor da tese e que nenhuma citação ou informação obtida a partir dela pode ser publicada sem a referência apropriada.

This copy of the thesis has been supplied on condition that anyone who consults it is understood to recognize that its copyright rests with its author and that no quotation from the thesis and no information derived from it may be published without proper acknowledgement.

ACKNOWLEDGEMENTS

Ao longo da elaboração do trabalho apresentado, recebi ajuda de valor incalculável dos meus orientadores, Professor Jaime Batista dos Santos, Professor

José Silvestre Silva e Professora Maria Alexandre de Albuquerque André. Em especial, agradeço a disponibilidade permanente para me auxiliar e guiar, tanto em relação ao trabalho realizado como em relação a possíveis melhorias a implementar.

Gostaria também de agradecer aos amigos que me acompanharam ao longo deste percurso e que me auxiliaram em momentos de dificuldade e festejaram comigo os momentos de felicidade.

Por último, agradeço aos meus pais que me educaram e suportaram em todos os momentos da minha vida e à minha irmã que sempre foi um exemplo para mim.

Rui Abreu

“If you do not believe you can do it then you have no chance at all.”

Arsène Wenger, in England

ABSTRACT

Cardiovascular diseases are one of the most important causes of death all over the world. In particular, atherosclerosis is a dangerous vascular condition difficult to diagnose at early stages and there is an urgent need for better techniques to diagnose patients at risk of stroke based on the measurements of the intima media thickness (IMT).

The objective of this work was to develop a new segmentation system for detecting the IMT of the common carotid artery (CCA). All the images are pre-processed in order to remove speckle noise and the region of interest (ROI) is automatically selected, using thresholding and connected-component analysis. The system is based in the first-order Gaussian derivative as edge detector on pre-processed images and this edge detector allows to enhance the lumen-intima and media-adventitia interfaces, whose distance between corresponds to the IMT.

The IMT values obtained were compared with measurements made by an expert and, in average, the difference between measurements was not significant but it has an associated standard deviation that can preclude medical applications.

Key-words: Ultrasounds, Carotid Artery, Atherosclerosis, Segmentation, Intima, Media, Adventitia;

RESUMO

As doenças cardiovasculares são uma das mais importantes causas de morte em todo o mundo. Em particular, a aterosclerose é uma doença difícil de diagnosticar em fases iniciais e há uma necessidade urgente de novas técnicas para diagnosticar pacientes em risco baseadas na medição espessura do complexo intima-media.

Este trabalho procura desenvolver um novo sistema de segmentação para a detecção da espessura do complexo intima-media em artérias carótida. Todas as imagens foram pré-processadas de forma a remover o efeito do ruído espectral, e a região de interesse é automaticamente selecionada usando *thresholding* e *connected-component analysis*. O sistema baseia-se na derivada de primeira ordem da função Gaussiana como detector das estruturas desejadas – interfaces lumen-intima e media-adventitia, cuja distância entre eles corresponde à espessura do complexo intima-media.

Os valores obtido foram comparados com medições realizadas por um especialista. Em média, a diferença entre medições não se mostrou significativa mas o seu desvio-padrão associado pode impedir a aplicação em situação médica.

Palavras-chave: Ultrasons, Artéria Carótida, Aterosclerose, Segmentação, Intima, Media, Adventitia;

LIST OF ABBREVIATIONS AND ACRONYMS

CEA	Carotid Endarterectomy
CCA	Common Carotid Artery
CVD	Cardiovascular Diseases
IM	Intima Media
IMT	Intima Media Thickness
IVUS	Intravascular Ultrasound
LI	Lumen Intima
MA	Media Adventitia
ROI	Region of Interest

LIST OF FIGURES

Figure 2.1 – Stages of the coronary artery disease [10]. 7

Figure 2.2 – Carotid arteries anatomy. The carotid arteries split into external and internal carotid arteries at the level of the superior margin of the thyroid cartilage. (adapted from the original belonging to Texas Heart Institute, www.texasheart.org) 9

Figure 2.3 - Types of wave reflections. Reflection can be categorized as either specular or diffuse. Specular reflectors are large, smooth surfaces, where the wave is reflected back in a singular direction. Conversely, a diffuse reflector cause the reflections to return in various directions in relation to the transmitted beam. 11

Figure 2.4 – Dependence of reflection strength on incident angle of the ultrasound wave. The nearer the incident wave is to 90° , the stronger will be the reflection. A: only 25% of the initial wave energy is reflected. B: 75% of the initial wave is reflected. 12

Figure 2.5 - An overview of an ultrasound system. The ultrasound beam reflection is received and then the signal is demodulated. The signal absolute value is taken and time-gain conversion and scan conversion are performed. Dynamic range conversion is part of the latter procedure [15].14

Figure 2.6 - Double line pattern characteristic of the ultrasound carotid images. A: Lumen-intima interface; B: Media-adventitia interface. 16

Figure 3.1 - Edge-tracking technique. A: B-mode image of the CCA; B: Despeckled and low passed image; C: Intensity profile of the column correspondent to the dashed line in B and D; D: Detected wall points. AD_N : Near wall adventitia. AD_F : Far wall adventitia. L: Lumen [26]. 20

Figure 3.2 - Left: theoretical representation of the expected gradient for a longitudinal ultrasound image of the CCA; Right: Real gradient obtained [27]. 21

Figure 3.3 - A: typical profile of the gray levels of a column of the ROI (near the far wall of the carotid artery). B: The same profile after the filtering process with the FOAM operator [29]. 22

Figure 3.4 - Possible snake erratic behavior in segmenting the LI and MA layers. (a): original image of the far wall. (b): Segmentation of Cheng's snake; (c): erratic behavior of a traditional snake; (d): ground truth obtained by manual segmentations [37].	26
Figure 3.5 - Average value and standard deviation of the pixel neighborhood intensity (normalized values). The pixels belonging to the carotid lumen are depicted in black and it is evident how that pixels are located in the first classes [39].	27
Figure 3.6 - Completely user-independent segmentation of the near and far carotid wall by a technique proposed by Molinari et al. [41]	29
Figure 3.7 - Right panel: representation of the ROIs selected in dynamic processing strategies. Each ROI contains the lumen, the intima-media structure and the adventitia layer. Left panel: assignment of the four boundaries [43].	30
Figure 3.8 - Flow chart of the procedure for (left) the identification of the arterial wall (in longitudinal and transverse sections) and the (right) estimation of the IMT [45].	31
Figure 3.9 - Representation of the integrated approach by Molinari et al. A: original image of the CCA. B: Seed points detected; C: Line segments obtained by connecting the seed points and discarding fragmented and misplaced lines. D: Final segmentation results [42].	32
Figure 4.1 – Typical images of the CCA. The image A presents a well-defined far wall along all the image, while the image B presents a good definition of the far wall only in the center of the image.	34
Figure 4.2 – Workflow of the segmentation.	34
Figure 4.3 – Border cropping of the images used.	36
Figure 4.4 - Image filtering. A: Original image; B: Conversion to grayscale; C: Median filtering [7x7].	36
Figure 4.5 - Double line pattern characteristic of the ultrasound carotid images. A: Lumen-intima interface; B: Media-adventitia interface.	37
Figure 4.6 – Intensity histogram of the image used as the main example.	38
Figure 4.7 - Result of the thresholding method over the image used.	39
Figure 4.8 - Candidate regions found with the technique applied.	40

Figure 4.9 – Division of each bounding boxes in three with same size.	41
Figure 4.10 – Redefinition of the sub-regions in order to include the far wall of the carotid artery.	41
Figure 4.11 - Initial segmentation. A: Result of the thresholding method applied in each sub-region. B: Segmentation of the biggest object in the image... 42	42
Figure 4.12 - Results of the filtering (B) and the first-order derivative of the Gaussian function (C) in the processed image (A) and in its intensity profiles. The intensity profiles are correspondent to the column represented by the dashed line in each image. NW: Near Wall; FW: Far Wall; L: Lumen; MA: Media-adventitia interface; LI: Lumen-intima interface.....	44
Figure 4.13 – Segmentation of the three sub-regions of the region of interest. 47	47
Figure 4.14 - Full Segmentation. A, B, C: sub-regions of the ROI.....	48
Figure 4.15 - Graphical User Interface implemented with the objective to facilitate the echography images processing.....	49
Figure 4.16 - The push button "Change Folder" allows to select the folder containing the images to process. It is set by default to the folder containing the echographies used in this work. The segmentation can be done following 2 different methods: Automatic and Semi-automatic (B) – after the option is selected, the push button “Start” starts the segmentation (D).	49
Figure 4.17 – Results display in the GUI. 1-3: Segmentation result for each sub-region; 4 – Original Image; 5 – Region of interest; 6 – Segmentation best result.	50
Figure 4.18 – The panel “Results and Diagnosis” present the IMT value and the respective diagnosis. The panel “View” allows to choose which image to display according to the numbering defined.	50
Figure 4.19 - Automatic segmentation of the CCA far wall. On the right, the classification is presented and the values of the mean and maximum thickness are presented.	51
Figure 4.20 - Semi-automatic segmentation of the CCA far wall. Two regions are presented and the user may choose the correct one, containing the far wall of the CCA. On the right, the classification is presented and the values of the mean and maximum thickness are presented.....	51

Figure 5.1 – Manual measurement of the image “CCA24.dcm” using ImageJ. 1: 0.061 cm; 2: 0.060 cm; 3: 0.060 cm.	54
Figure 5.2 – Automatic segmentation of the image “CCA24.dcm”.....	55
Figure 5.3 – Automatic segmentation failure in an image with thyroid nodules. Image “CCA81.dcm”. Results obtained using MatLab [49].	56
Figure 5.4 – Bland-Altman comparing each of the 4 relationships defined. The mean difference between groups as well as the limits of agreement for a confidence of 95% are shown. Values in centimetres. Graphs obtained using GraphPad Prism 6 [52].	58

LIST OF TABLES

Table 5.1 - Average and standard deviation of each of the 4 comparisons performed. All values are in centimetres. Data obtained using GraphPad Prism 6 [52].	58
Table 5.2 – P-value of Mann-Whitney test for each relationship. Data obtained using GraphPad Prism 6 [52].	59
Table 5.3 – Pearson’s Correlation Coefficient for each relationship. Data obtained using GraphPad Prism 6 [52].	60

TABLE OF CONTENTS

1 INTRODUCTION.....	1
1.1 MOTIVATION AND THESIS OBJECTIVE	1
1.2 THESIS OVERVIEW.....	2
2 THEORETICAL CONCEPTS.....	5
2.1 CARDIOVASCULAR DISEASES	5
2.1.1 <i>Atherosclerosis</i>	5
2.1.2 <i>Carotid Artery</i>	8
2.2 MEDICAL IMAGING TECHNIQUES.....	9
2.2.1 <i>Angiography</i>	9
2.2.2 <i>Ultrasound Imaging</i>	10
2.3 OTHER ULTRASOUND METHODOLOGIES	18
3 CAROTID SEGMENTATION ALGORITHMS	19
3.1 EDGE TRACKING AND GRADIENT-BASED TECHNIQUES.....	19
3.2 DYNAMIC PROGRAMMING TECHNIQUES	22
3.3 SNAKED-BASED SEGMENTATION.....	23
3.4 LOCAL STATISTICS AND SNAKES	27
3.5 NAKAGAMI MODELING.....	29
3.6 HOUGH TRANSFORM	30
3.7 INTEGRATED APPROACH.....	31
4 MATERIALS AND METHODS.....	33
4.1 ACQUISITION OF DATA	33
4.2 METHODOLOGY	34
4.2.1 <i>Pre-processing</i>	35
4.2.2 <i>Automatic selection of the region of interest</i>	36
4.2.3 <i>Segmentation</i>	43
4.3 GRAPHICAL USER INTERFACE (GUI)	48
5 RESULTS AND DISCUSSION.....	53
5.1 MANUAL MEASUREMENTS.....	53
5.2 AUTOMATIC MEASUREMENTS	54
5.3 AMBIGUOUS RESULTS.....	56
5.4 STATISTICAL ANALYSIS.....	57

5.4.1 <i>Bland-Altman plot</i>	57
5.4.2 <i>Mann-Whitney test</i>	59
5.4.3 <i>Pearson’s Correlation Coefficient</i>	59
5.5 SUMMARY	60
6 CONCLUSIONS AND FUTURE WORK	61
6.1 CONCLUSIONS.....	61
6.2 FUTURE WORK.....	62
7 REFERENCES.....	65
APPENDIX A	71
APPENDIX B	75
APPENDIX C	77

1 INTRODUCTION

1.1 MOTIVATION AND THESIS OBJECTIVE

Cardiovascular diseases are one of the most important causes of death all over the world. In particular, atherosclerosis is a dangerous vascular condition difficult to diagnose at early stages. A progressive buildup of atheromatous plaques on the walls of blood vessels due to deposits of fatty materials is the main process associated with atherosclerosis development that can thereafter eventually cause stenosis (abnormal narrowing) of the blood vessel, embolisms, and lead to death.

The carotid artery is one of the locations of particular concern for the atherosclerosis diagnosis once it carries blood to the head. The carotid bifurcation region, where the common carotid artery (CCA) branches off into two arteries, is a particularly vulnerable spot for plaque formation. At advanced stages of atherosclerosis in this region, a portion of plaque can break and be carried with the bloodstream to the brain, blocking the blood supply to the brain tissue and, which can injure it due to ischemia.

Computer-aided diagnosis is a successful and relevant field of biomedical engineering with great development in recent decades. A multitude of tedious, time-consuming and otherwise unmanageable medical tasks can be made feasible by combining medical expert knowledge with signal processing and pattern analysis tools. In particular, a wide variety of medical image processing techniques have been devised in order to solve problems of registration of images from different sources, their transformation into a more

informative form, or delineation of regions of interest (ROI) using automatic segmentation. This often enables improved diagnosis of various medical conditions or makes it more cost-effective and less invasive.

Once it is a pathology highly associated with the zone where blood flux is disturbed, several ways to detect and understand the process of the formation of the atheromatous plaque has been studied. One larger field of study in this thematic is focused on B-mode carotid imaging, because it is one of the most affordable, harmless and most widely used image systems in the world.

The diagnostic of the disease can be performed by the characterization of the atheromatous plaque and its degree of obstruction. In the carotid artery, the characterization is done by the measurement of the intima-media complex. Nowadays, ultrasounds are used as the main diagnosis method that can be followed by an angiography to confirm the diagnostic and decide about a possible surgery.

The aim of this thesis is to propose a method of automatic segmentation of the carotid artery wall, and the measurement of the intima-media thickness (IMT), in order to provide a diagnosis accordingly to the result.

1.2 THESIS OVERVIEW

The structure of the remaining part of this thesis is as follows. First, theoretical concepts about cardiovascular diseases and medical imaging techniques are introduced and explained in detail in **chapter 2**. Then, in **chapter 3**, several algorithms applied in order to measure the IMT are presented and discussed, with the aim of evaluating the approach with better results and performance, accordingly to its measurement error and automation degree.

The **chapter 4** explains the developed algorithm in this work, explaining all the steps applied in the automatic segmentation with the respective changes in the image characteristics. The results of the segmentation are organized and displayed in a graphical user interface, which is also described in this chapter.

In **chapter 5**, the results of applying the proposed automatic segmentation over the dataset used in this work are presented along with the

statistical interpretation of them. This statistical results allow evaluating the algorithm performance by comparing the IMT measures with a ground-truth provided by an expert.

The **chapter 6** summarizes the thesis and presents the achieved conclusions. The future perspectives related with this subject are also covered in this last chapter.

2 THEORETICAL CONCEPTS

2.1 CARDIOVASCULAR DISEASES

The industrialization, brought by the revolution that occurred in the XVIII and XIX centuries, changed the death causes all over the world but mainly in the most advanced societies. The nutritional deficiency problems and the infectious diseases have been decreasing, while chronic diseases such as cardiovascular diseases (CVD), cancer and diabetes began to take priority as a health problem [1].

CVD are currently a major cause of morbidity and mortality worldwide. The World Health Organization estimates that 17.5 million people died from cardiovascular diseases in 2012, which represents 31% of all deaths across the globe [2], [3].

The main risk factors for CVD are tobacco, physical inactivity, diet, obesity, high blood cholesterol, high blood pressure and alcohol consumption [4], [5]. Also the family history and age should be taken into account being, in particular, patients with diabetes mellitus one of the most important risk group [6].

2.1.1 ATHEROSCLEROSIS

Atherosclerosis is one of the most prominent cardiovascular diseases and it is characterized by inflammation of blood vessels due to the accumulation of mainly lipids in the artery walls, which is the origin of the atheromatous

plaque [7]. The disease progression stages and their characteristics are presented in the following paragraphs.

Large arteries are bounded by a monolayer of endothelial cells that form tight junctions, insulating the vessel wall from the blood. Underneath there is a region called the intima, which consists mainly of proteoglycans and collagens. This is followed by layers of smooth muscle cells and then an outer region – the adventitia – comprising fibrous elements (image A of the figure 2.1) [7], [8].

The initial stage of atherosclerosis is characterized by the accumulation of low density lipids in the intima region. This accumulation causes immune system to respond by secreting monocytes that give rise to macrophages (image B of the figure 2.1). These macrophages act on low density proteins, creating cholesterol-engorged “foam cells”, a hallmark of early atherogenesis (image C of the figure 2.1) [8].

A necrotic core of cholesterol and cellular debris is created as some of these foam cells die. This is accompanied by a migration and proliferation of smooth muscle cells, which form a fibrous cap that overlies the core. Depending on the thickness of the fibrous cap, it is possible to be formed a stabilized plaque, with a thick fibrous cap (image D of the figure 2.1), or a vulnerable plaque, with a thin fibrous cap (image E of the figure 2.1) [8].

The most common cause of myocardial infarction is the rupture of an atherosclerotic lesion, leading to the formation of a thrombus that can block the blood flow (image F of the figure 2.1). This kind of stroke accounts for approximately 75% of all strokes [9]. The vessel stenosis is also possible if the atheroma is able to continue its growth without reaching its rupture, decreasing the lumen area and partially or totally (ischemia) blocking the blood flow [3], [7].

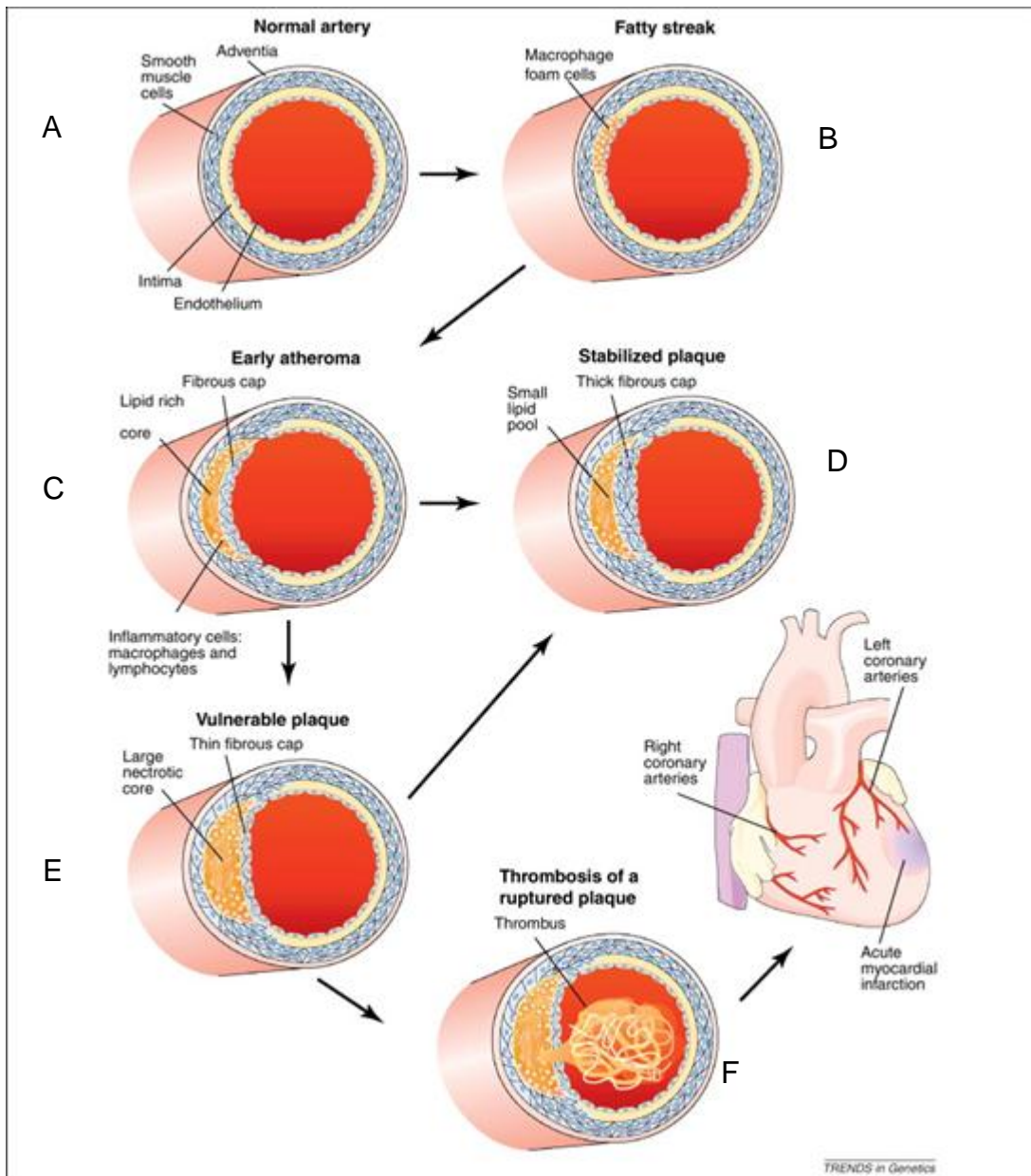


Figure 2.1 – Stages of the coronary artery disease [10].

Spontaneous regression can occur on early stages of the disease, but intermediate and advanced ones appear to be continuously progressive [5]. Thus, the treatment is not always a straightforward decision since the potential benefit of the surgery must be weighed against the risks of the surgery. The degree of stenosis is measured as the difference between the largest and the smallest area of the artery in relation to the largest one and it can play an important role in this decision. For a degree of stenosis smaller than 30%, medical therapy is preferred, while between 30% and 70% it has not been determined the best therapy yet. Higher degrees of stenosis demand a surgery.

The IMT is also an important indicator of early stages of the disease and it will be studied in depth later [11].

Different options are available to treat atherosclerosis. They include lifestyle changes, medication, and surgery. Lifestyle changes imply in following a healthy diet to reduce the high blood pressure or high blood cholesterol and to maintain a healthy weight, and increasing the physical activity, quitting smoking, and managing stress. Medication includes drugs to lower the cholesterol level or blood pressure and medicines to prevent formation of blood clots. In case of severe atherosclerosis, surgical procedures are carotid endarterectomy (CEA) or carotid artery stenting. In a CEA procedure, an incision is made on the neck, then the carotid artery is opened and the atherosclerotic plaque buildup inside is surgically removed, restoring normal blood flow to the brain. Carotid artery stenting is a minimally invasive procedure carried out through catheter techniques. Using catheters, a small balloon is inflated in the narrowed area of the carotid artery opening it for improved blood flow. A stent is then inserted into the newly-opened area to help keeping the artery from narrowing or closing again [12].

2.1.2 CAROTID ARTERY

The head and neck receive the majority of its blood supply through the carotid arteries. Thus, due to its importance, the occurrence of atherosclerosis in these arteries may have severe consequences.

The right CCA arises from the brachiocephalic trunk while the left one branches directly from the arch of aorta. The carotid arteries then split into external and internal carotid arteries at the level of the superior margin of the thyroid cartilage (figure 2.2). This bifurcation is one of most susceptible places for atheromatous plaques to grow, once the blood flow rates have rapid variations and there is a significant shear stress. The external carotid arteries supply the areas outside the skull, while the internal carotid arteries lead the blood to the brain, eyes and forehead [3], [11].

The brain uses about 15% of total blood stream and consumes 20% of the whole oxygen and glucose of the organism, due to huge energy demand. Its metabolism requires a high amount of oxygen and a gap of just 10 seconds on

oxygen supply causes loss of conscience. Besides, if the absence of oxygen goes beyond 4 minutes, such can result in severe and permanent brain injuries [7].

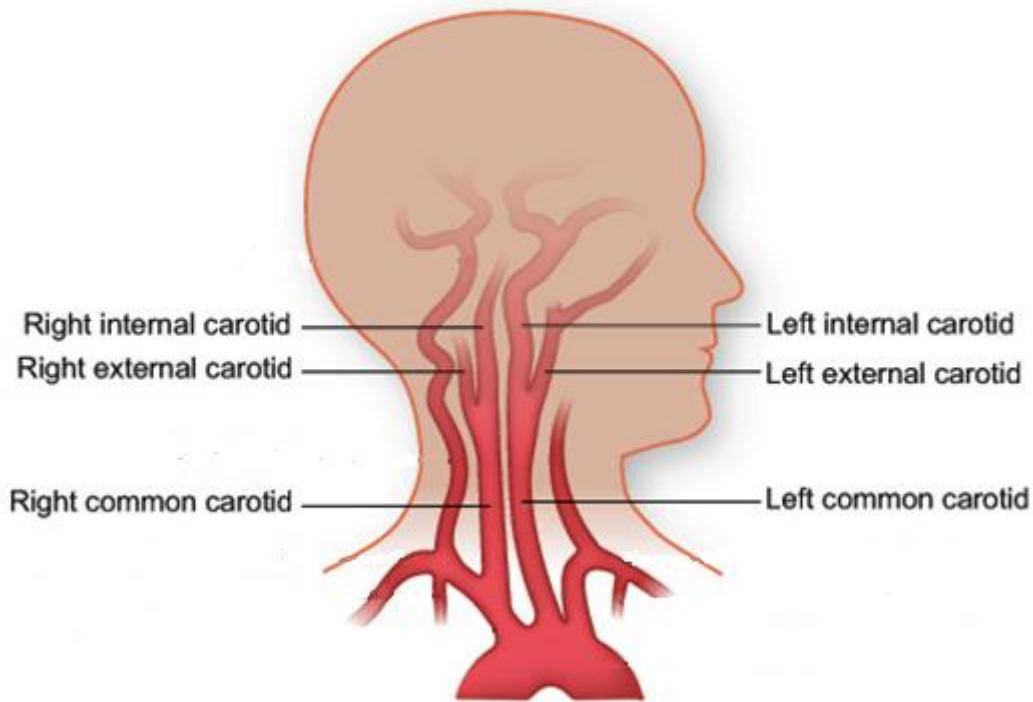


Figure 2.2 – Carotid arteries anatomy. The carotid arteries split into external and internal carotid arteries at the level of the superior margin of the thyroid cartilage. (adapted from the original belonging to Texas Heart Institute, www.texasheart.org)

2.2 MEDICAL IMAGING TECHNIQUES

Medical imaging refers to the process of creating a visual representation of the interior of a body, permitting its analysis in order to aid the medical intervention. Those images try to reveal internal structures hidden by the skin and bones, making possible to identify abnormalities. In particular, medical imaging techniques provide the means to directly examine the carotid artery, allowing the diagnosis about the atheromatous plaque presence. Some of the most used techniques are presented below, as well as their advantages and handicaps.

2.2.1 ANGIOGRAPHY

Angiography is an imaging technique which allows the visualization of blood vessels by injection of a contrast agent into the bloodstream. This makes

the blood more discernible in the image, highlighting any narrowing or occlusions in the vessel images [3].

Traditionally, the most used angiography modality is x-ray imaging, in which a contrast agent that absorbs x-rays is injected into the bloodstream and the image acquisition is carried out afterwards. This technique provides a two-dimensional image, however a three-dimensional one can be acquired by taking a series of x-rays at regular spacing or angles, which is called Computed Tomography Angiography.

Angiography is widely available and cost-effective but the contrast material can produce a severe allergic reaction. Moreover, patients with advanced diabetes or kidney problems should avoid this treatment. Even knowing that it reaches a 70-99% accuracy on the diagnosis of severe stenosis of carotid, the associated risk demands an alternative. A viable and safer alternative is the ultrasound imaging, in which the developed work is based on and presented below [9].

2.2.2 ULTRASOUND IMAGING

ULTRASOUND PRINCIPLES

An ultrasound wave is an oscillatory variation in pressure, which frequency is above the range of human hearing. As any wave, it possesses certain parameters such as wavelength and energy but, unlike electromagnetic waves, it needs a medium to travel through. Compressions and rarefactions are produced while the wave travels depending on the medium properties, like density and elasticity [13].

As it travels through a complex object, some energy is lost gradually due to absorption, where the heat energy dissipation is the most important process. Whenever the acoustic properties of media changes, some energy of the ultrasound wave is reflected back, forming the basis of an ultrasound image [13].

The interface created by two different media has an associated acoustical impedance that is proportional to the difference of the sound velocities on the medium. This impedance gives rise to the reflection of a portion of the energy, resulting in specular reflection, while the remainder will

travel further. The ultrasound wave can also interact with very small objects that can create a diffuse scattering of the incident wave, which, unlike the specular reflection, has no predominant orientation, resulting in an incoherent interference component in the resulting image. The differences between these two types of reflections can be seen in figure 2.3 [13].

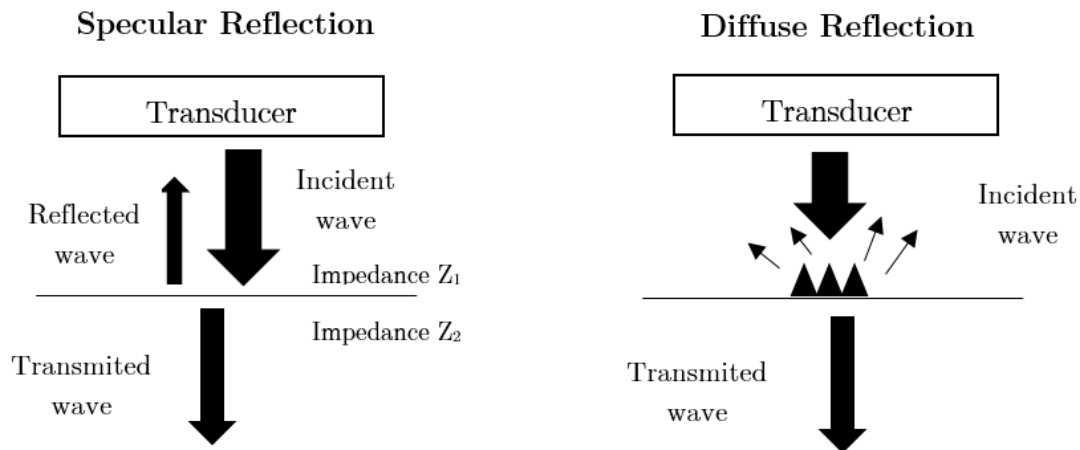


Figure 2.3 - Types of wave reflections. Reflection can be categorized as either specular or diffuse. Specular reflectors are large, smooth surfaces, where the wave is reflected back in a singular direction. Conversely, a diffuse reflector cause the reflections to return in various directions in relation to the transmitted beam.

The reflection coefficient relates the acoustical impedances of two media and is given by the following expression:

$$R = \frac{Z_2 - Z_1}{Z_1 + Z_2}, \quad (2.1)$$

where Z_1 and Z_2 represent acoustic impedance of two different media. The expression suggests that the larger the difference between Z_1 and Z_2 , the higher the percentage of energy will be reflected [13]. Once that reflection reduces the ultrasound wave energy, a strong reflection will result in bright boundaries in the ultrasound image, but any deeper tissue interfaces will be exposed to a wave with less energy. This phenomenon, in concern to ultrasounds, is known as acoustic shadowing and degrades the quality of the image [13].

Another problem about ultrasound waves is related to the incident angle on the interface boundary. If that angle is different of 90° , it is possible to apply the Snell's law and the angle, as well as the energy of the reflected and refracted waves, will be proportional to the incident angle, as shown in the figure 2.4. This dependence has an important impact on the nature of the images produced by the ultrasonic devices: they are orientation-dependent [13].

When tissue boundaries are oriented in an axial or nearly axial direction, the result images will have weak and discontinuous interfaces [13].

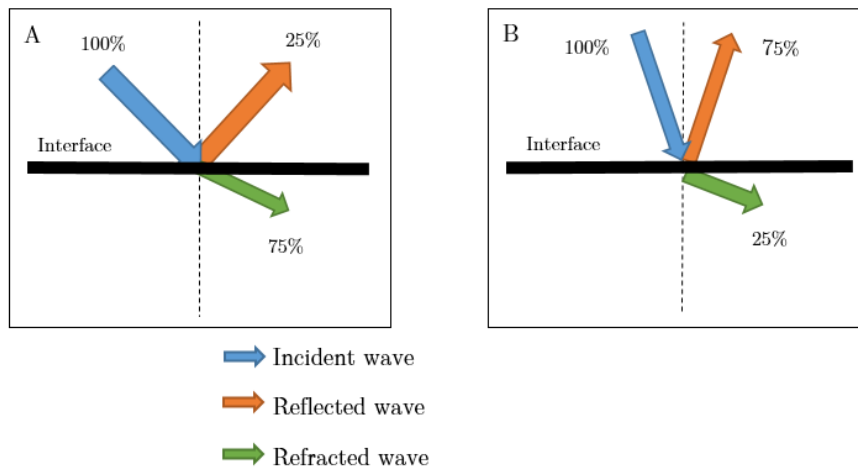


Figure 2.4 – Dependence of reflection strength on incident angle of the ultrasound wave. The nearer the incident wave is to 90°, the stronger will be the reflection. A: only 25% of the initial wave energy is reflected. B: 75% of the initial wave energy is reflected.

SIGNAL GENERATION AND DETECTION

Piezoelectric effect ceramics suffer deformation when an electrical voltage is applied to them, generating mechanical waves. Conversely, when submitted to a pressure they generate a voltage. These ceramics are the active elements of the ultrasonic transducers [13].

The ultrasound image production is based on the time needed to send and receive a wave. The result is a one-dimensional depth profile, known as A-mode scanning, formed by only the waves reflected in the incident direction [13].

While A-mode scanning generates a one-dimensional depth profile, a two-dimensional image can be obtained by collecting several A-scans, rotating or linearly translating the transducer, and grouping all profiles. That is called B-mode scanning and can be implemented with one transducer or with a transducer array instead. This array can be linear or curved and allows creating a two-dimensional image with a single scan [13].

The frequency of waves determines the image resolution. The higher it is, the higher the resolution will also be. However, resolution is inversely proportional to the depth to explore [3].

POST-PROCESSING

The signal received by the transducer must be further processed to be displayed on a screen or stored in a digital form for later analysis. These procedures are normally applied in the ultrasound system's hardware immediately upon the signal acquisition [3].

The first step is to demodulate the signal obtained. The result is the envelope image, which is appropriate to display, after the post-processing [14].

Since the waves lose energy as they propagate deeper results in an image with very strong structures, corresponding to tissues closer to the transducer, and severely weakened structures for tissues at higher depths, it is strictly necessary to compensate this phenomenon. With this objective it is applied a time-gain compensation, consisting on an amplification of the reflected wave. The amplification coefficient increases with time since transmission, and thus with the distance of the imaged tissue. This compensation should be adjusted depending on the tissue being imaged [14].

Tissue interfaces closer to the transducer will produce high amplitude reflections, while deeper or weaker boundaries will result in much smaller amplitudes. In addition, specularly reflected echoes have much higher amplitude when compared to the ones from scattering, causing the strongest reflections to largely dominate the image. The solution to this problem is to compress the dynamic range, which is done by the following type of function:

$$f(x) = A \log(Dx + B), \quad (2.2)$$

where the user-adjustable parameter D controls compression and constants A and B depend on the signal's digital resolution [14]. The figure 2.5 represents the ultrasound image acquisition workflow:

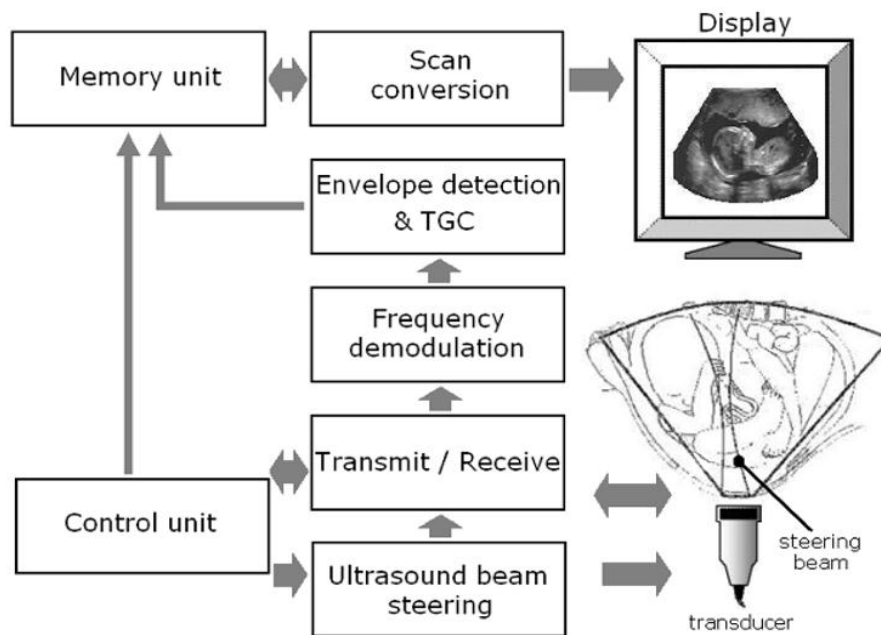


Figure 2.5 - An overview of an ultrasound system. The ultrasound beam reflection is received and then the signal is demodulated. The signal absolute value is taken and time-gain conversion and scan conversion are performed. Dynamic range conversion is part of the latter procedure [15].

SPECKLE PATTERN

Some phenomena like acoustic shadowing can affect the quality of the acquired ultrasound image. In this section it is described the speckle pattern, which demands an additional post-processing step to improve the quality of the ultrasound image.

The reflected echoes may be grouped into two types. Specular reflections are related to strong, relatively smooth and long interfaces between two tissues of different echogenicity. Scattered reflections created by more irregular boundaries and by objects that are small compared to the wavelength of the wave result in a speckle interference pattern which can be treated from the viewpoint of the stochastic signal analysis [16].

Inside a homogeneous section of the imaged tissue, there may be multiple small-scale objects and the accumulation of these different scatterings influences the resulting speckle pattern. This contamination of the ultrasound envelope image is often defined using the following noise model [16]:

$$I(x) = u(x)v(x) + e(x) \quad (2.3)$$

The spatial coordinate is defined by x , I is the observed envelope image, u is the original image, v and e are, respectively, the multiplicative and

additive components of speckle pattern. This is not the only possible model and it has limitations, although it had been widely used [16].

The logarithmic compression applied to the echo signal envelope in order to fit it in the display range affects the speckle noise statistics in such a way that the local mean becomes proportional to the local variance rather than the standard deviation. More specifically, logarithmic compression affects the high intensity tail of the Rayleigh and Rician probability density function more than the low-intensity part. As a result, the speckle noise becomes very close to white Gaussian noise corresponding to the uncompressed Rayleigh signal [17].

ULTRASOUND IMAGING APPLIED TO CCA

The development of non-invasive methods for imaging atherosclerosis has resulted in a paradigm shift in our understanding and management of vascular disease by enabling its identification at a preclinical stage [18].

Ultrasound imaging is cost-effective and safe but it may suffer from sound-reflecting properties of tissue, creating acoustic shadowing, speckle noise and discontinuous tissue boundaries. It is used in vascular medicine for two main purposes: to guide invasive medical procedures and to visualize the degree of stenosis for diagnosis of atherosclerosis. The location of the carotid artery makes it suitable for ultrasound imaging, as it runs parallel and near to the surface of the neck. The possibility to repeat the process as often as required, without danger, is a very important characteristic of the ultrasound image acquisition as well [2], [3].

The first time ultrasound imaging was applied on carotid arteries was in 1986 by Italian researchers. They reported the results of an in vitro study of 18 human aorta and common carotid arteries, which compared direct measurements of arterial wall thickness and microscopic examination with B-mode real-time imaging of those same specimens. They described a characteristic B-mode image of the arterial wall composed of two parallel echogenic lines separated by a hypoechoic space. The distance between the two lines did not differ significantly from the IMT measured on pathologic examination, leading the researchers to suggest that B-mode imaging could present a useful approach to the measurement of the IMT in vivo [2]. A

longitudinal view of the CCA is presented in the figure 2.6 as well as the double line pattern relative to intima-media complex.

It is relevant to note that, most likely due to the different order in which the interfaces of the intima-lumen and media-adventitia are exposed to the incident ultrasound beam, the B-mode images of the near (more superficial) and far (deeper) walls are different. All experiments are, usually, performed only on far walls because they could provide better results [19].

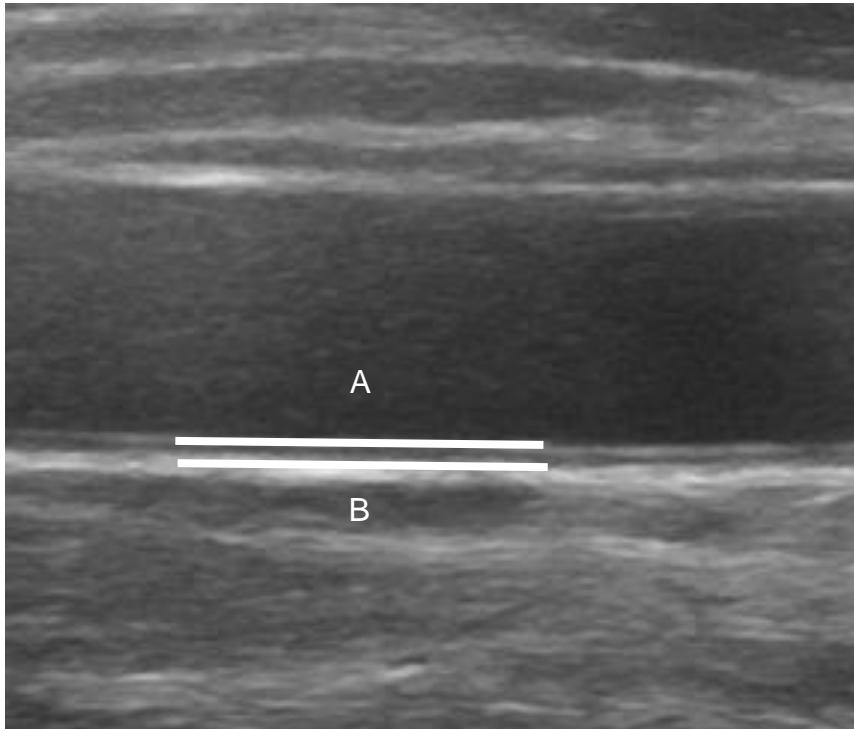


Figure 2.6 - Double line pattern characteristic of the ultrasound carotid images. A: Lumen-intima interface; B: Media-adventitia interface.

INTIMA-MEDIA THICKNESS

The first morphological irregularities of arterial walls can be visualized by B-mode ultrasonography. Accordingly, ultrasound has been used in a number of studies to monitor the IMT of the carotid arteries, a measurement which has been shown to be associated with cardiovascular risk factors and with the incidence of cardiovascular disease [19].

In ultrasound images, the carotid artery wall is depicted as three separate layers: intima, media and adventitia. The measurements of carotid IMT are made on these images and they are used to assess the extent of atherosclerosis and work as a biomarker for the future risk of cardiovascular disease and stroke [20].

The IMT is defined as the distance from the lumen-intima interface, represented as A in figure 2.6, to the media-adventitia interface, represented as the B in figure 2.6 [21]. The intima-media (IM) complex can easily be distinguished from the surrounding tissue in ultrasound images and the distinct borders allow for manual as well as automatic measurement of the IMT [20]. With increasing age, this pattern has been shown to thicken, in a uniform way. However, this thickening is accelerated and enhanced in the presence of risk factors [19].

The Mannheim Carotid Intima-Media Thickness Consensus (2004-2006) tries to solve the important issue of standardization of carotid IMT measurements and seeks to clarify problems related to the classification of early atherosclerotic lesions. The consensus recommends the following definitions [19]:

- 1) IMT is a double-line pattern visualized by echotomography on both walls of the common carotid arteries in a longitudinal image. It is formed by two parallel lines, which consist of the leading edges of two anatomical boundaries: the lumen-intima and media-adventitia interfaces [19];
- 2) Plaque is a focal structure encroaching into the arterial lumen of at least 0.5 mm or 50% of the surrounding IMT value, or demonstrates a thickness >1.5 mm as measured from the media-adventitia interface to the intima-lumen interface [19];

These definitions will allow the classification of the vast majority of carotid lesions observed with ultrasounds. The consensus recommends that IMT should be measured preferably on the far wall, and it also defends that it is plausible that the mean IMT values are less susceptible to outliers and are the best indicators in most cases [19].

The measurement of the intima and media combined layers, as determined by high-resolution B-mode ultrasonography, is now widely recognized as a useful tool for early identification for systemic atherosclerosis. IMT evaluation can identify individuals at risk for future cardiovascular events, and also evaluate the effectiveness of different therapy modalities for controlling morbidities that lead to the development of atherosclerotic-based diseases by identifying regression in IMT values after such interventions [22].

2.3 OTHER ULTRASOUND METHODOLOGIES

Beside the ultrasound B-mode imaging, other types of ultrasound imaging are used on this purpose, like Intravascular Ultrasound (IVUS) and Doppler Ultrasound [3].

IVUS images the carotid artery from the inside through an incision. A catheter is inserted into the artery with an ultrasound probe as its tip. It is a highly accurate alternative to angiography and has been used to evaluate the efficacy of drug therapies in treating atherosclerosis. However, the primary drawback of this surgical technique is its invasiveness, as well as the high cost [23].

Doppler ultrasound uses the Doppler Effect, which is related to the change in frequency of a wave for an observer moving relative to its source, to measure the blood flow velocity in the artery. These measurements can be used to estimate the actual velocity or to color-code it and overlay with the ultrasound image itself. The frequency spectrum obtained from the returning signal can also be analyzed to provide information about the blood flow dynamics [3].

3 CAROTID SEGMENTATION ALGORITHMS

3.1 EDGE TRACKING AND GRADIENT-BASED TECHNIQUES

The first attempt to perform carotid wall segmentation was based on edge-detection [24], [25]. The CCA ultrasound image appearance drove this first approach: as depicted in figure 3.1, the CCA can be defined as a dark region (the lumen) surrounded by two similar patterns (the near and far walls), consisting each one on two bright lines (intima-media and media-adventitia interfaces). Since the adventitia layer is usually very bright, due to its dense and fibrous composition, it is relatively easy to locate the lumen-intima interface such as the media-adventitia interface (image C in the figure 3.1). The distance between these two borders corresponds to the IMT estimation. It is applied a despeckle filter that highlights the peaks and makes the lumen a homogeneous region with low intensity pixels (image C in the figure 3.1) [3], [26]. This was the basis used by Touboul et al. on the IMT measurement approach, applied in several multi-centric clinical and epidemiological studies.

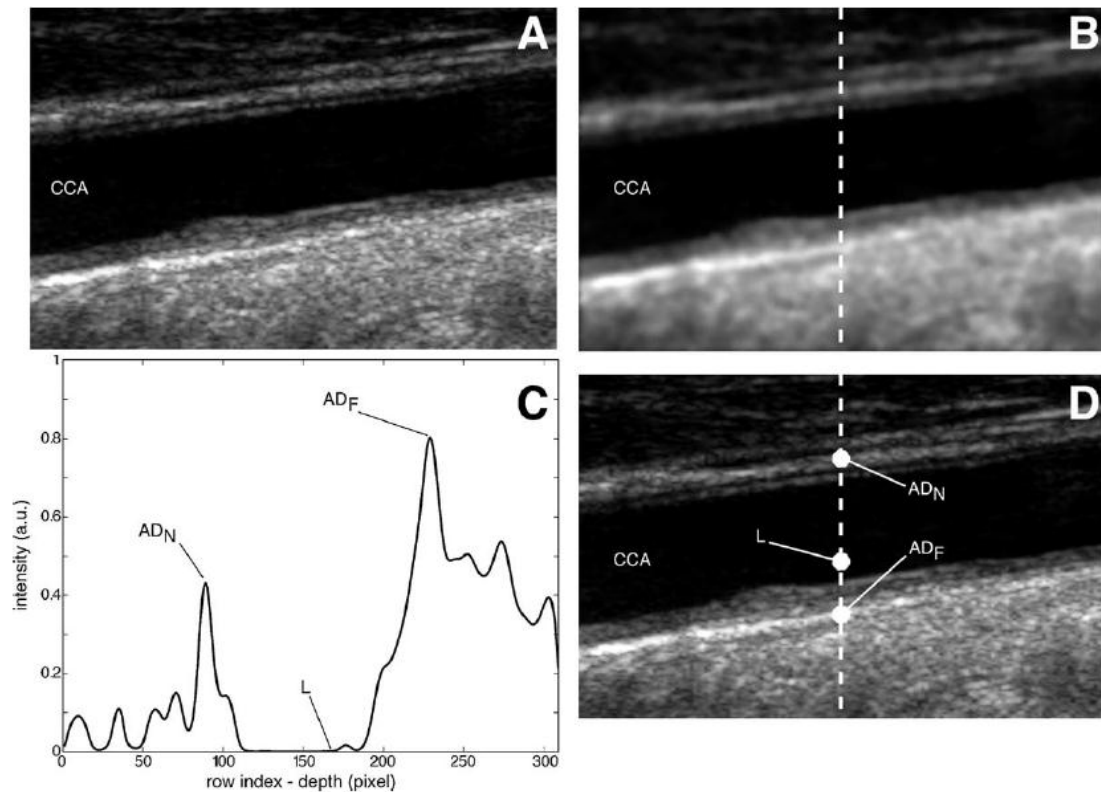


Figure 3.1 - Edge-tracking technique. A: B-mode image of the CCA; B: Despeckled and low passed image; C: Intensity profile of the column correspondent to the dashed line in B and D; D: Detected wall points. AD_N: Near wall adventitia. AD_F: Far wall adventitia. L: Lumen [26].

In 2001, Liguori et al. proposed a technique based on edge detection that used the vertical intensity profiles of a B-mode image and the respective gradient. The intensity profile refers to the pixel intensity in each column of the image and the ideal gradient of this profile is shown in figure 3.2 and it considers the artery as horizontally placed in the B-mode image. It also assumes that all the pixels of the artery lumen are black and that the carotid wall layers originate with gradient transitions. The first set of transitions (A in figure 3.2) is relative to the near wall, while the second (B in figure 3.2) is relative to the far wall [27].

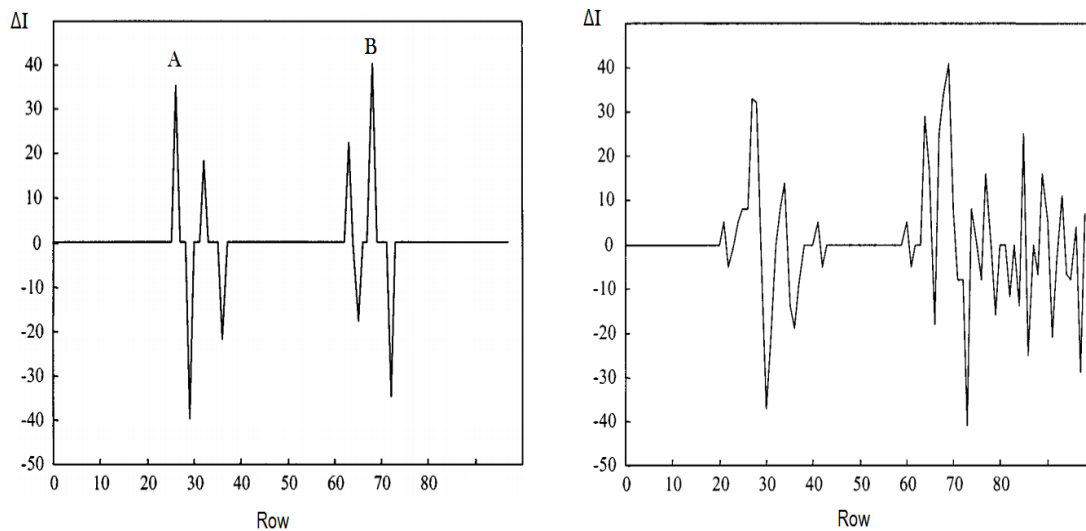


Figure 3.2 - Left: theoretical representation of the expected gradient for a longitudinal ultrasound image of the CCA. A: Near wall of the CCA. B: Far wall of the CCA; Right: Real gradient obtained [27].

However, due to noise, the intensity gradient measured is different from the theoretical one (see right side of figure 3.2). In order to solve this problem, Liguori et al. applied a statistical thresholding to reduce the noise before computing the image gradient. The authors defined the pixels corresponding to blood or other non-reflective substances as, at least, 60% of the total image pixels, while the remaining 40% relate to the brighter pixels, corresponding to the artery walls [27]. This segmentation approach was evaluated in 30 images and it had an uncertainty of $20\mu\text{m}$ on the IMT measurement, which is negligible for medical application. Nevertheless, this technique lacks full automation, once it requires the selection of the image portion where it will act.

In 2005, Stein et al. reported the results of a comparison between the IMT measurements made with and without the aid of a computed system. By using an expert and one novice operator for performing several IMT measurements, it was clear that the computer-aided IMT measurements were faster, more reproducible, accurate and independent on the operator skill [28].

The most performing and innovative gradient-based approach was proposed by Faita et al. on its recent work [29]. They tried solving the superimposed noise problem, which precludes a proper location of the LI and MA transitions, by applying a first-order absolute moment edge operator (FOAM) and a pattern recognition approach. Let $f(x,y)$ be the gray map of an image, and let Θ be a circular domain with area A_Θ whose center is the point with coordinates x,y ; The FOAM operator was defined as [29]:

$$e(x, y) = \frac{1}{A_\theta} \int_{\theta} \int_{\theta} |f(x, y) - f(x - \tau_x, y - \tau_y)| d\tau_x d\tau_y \quad (3.1)$$

When equation 3.1 is computed at a discontinuity point of an image, it gives rise to a local maximum. The figure 3.3 shows the shift on the intensity profile due to FOAM operator application [29].

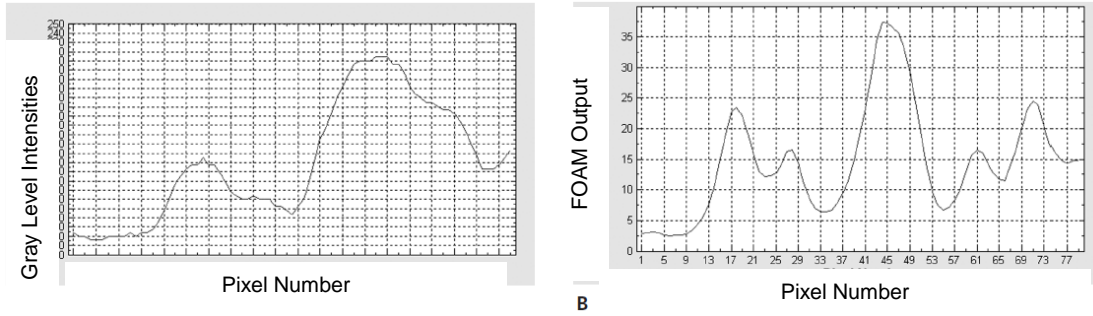


Figure 3.3 - A: typical profile of the gray levels of a column of the ROI (near the far wall of the carotid artery). B: The same profile after the filtering process with the FOAM operator [29].

The search algorithm then performs the segmentation by finding the LI interface, which corresponds to the first maximum of each intensity profile, starting from the center of the lumen. Then, the next maximum, which has an intensity higher or equal to the first one, is assigned as part of the MA interface. Finally, a least square regression line is computed to fit the points of each interface, and the points that are farther from the line are discarded [29].

The methodology was evaluated with 50 images and the overall performance was very high, with an IMT measurement error of 10 μm . It can be used in real-time, hence it is suited for clinical application. However, some problems were detected in processing curved vessels and full automation was not implemented, since it needs manual selection of a region-of-interest [29].

3.2 DYNAMIC PROGRAMMING TECHNIQUES

In order to reduce the variability introduced by the ultrasound system operators, dynamic programming techniques were introduced in early 1990s [30]–[34].

The first dynamic programming approach was introduced by Wendelhag et al. [34], which combines multiple measurements of echo intensity, intensity gradient and boundary continuity to create a cost-function. The boundary detection algorithm inspects all points in the image, considering

all possible lines that may form the interfaces, and favors the ones that minimize the cost-function. Therefore, points being located at the interfaces between different artery layers were expected to be associated with a low-cost, whereas points located far from the interfaces were associated with a high-cost [30]–[34].

As mentioned before, the cost function included three main terms: echo intensity, intensity gradient and boundary continuity. It can be described as

$$C(i) = w_1 c_1(i) + w_2 c_2(i) + w_3 c_3(i - 1, i), \quad (3.2)$$

where w is the weight factor, i is the pixel position, c_1 is the echo intensity, c_2 is the intensity gradient and c_3 is the boundary continuity. The cost function is computed at every pixel i and those consecutive pixel positions, resulting in the lowest total cost, will form the detected interface. This means that higher intensity, stronger gradient and better continuity correspond to lower value of the cost function.

This new automated system was tested in 50 images and it produced results less dependent on the experience of the reader, decreasing variability and greatly increasing the speed of measurements. The IMT measurement error by this technique was better than $40 \pm 36\mu\text{m}$. The major advantage of this methodology was complete automation but its computational cost was remarkable, since it needs to process all image pixels [30]–[34].

In 2000, Liang et al. improved the above mentioned algorithm by estimating the global position of the artery in the image on a coarse scale, thus decreasing the amount of pixels to analyse. A precise position of the wall layers was then estimated in a fine scale, ensuring accurate performance. This technique improved the computational burden while maintaining the segmentation performance [32].

3.3 SNAKED-BASED SEGMENTATION

The snakes, or active contours, are deformable models that act like a set of vertices connected by line segments. These vertices can evolve under the action of different forces [26].

A two-dimensional snake can be defined as a parametric contour represented by $v(s) = [x(s), y(s)]$, where (x, y) denotes the spatial coordinates

of an image and s represents the parametric domain. The snake adapts itself by a dynamic process that minimizes a global energy function defined as follows [35].

$$E_{snake}(v) = E_{int}(v) + E_{ext}(v) \quad (3.3)$$

where $E_{int}(v)$ is the internal energy of the snake and $E_{ext}(v)$ is the external driving energy. For a general application, the internal energy depends on some constraints that are imposed to the snake and can be formulated as [35]:

$$E_{int}(v) = \int_0^1 \{\alpha(s)|v'(s)|^2 + \beta(s)|v''(s)|^2\} ds \quad (3.4)$$

where $\alpha(s)$ and $\beta(s)$ are the snake elasticity and rigidity coefficients, respectively. The internal energy prevents the snake from twisting or bending in an excessive way, better preserving the morphology of the features of the image [35].

The external driving energy typically depends on relevant features of the image, like borders or lines. In most of the snake-based algorithms, this energy is modeled by using the local image gradients. Thus, the best snake points are found by moving them towards the features of the image while remaining constrained by the internal forces and the snake reaches its equilibrium condition when the energies in the equation 3.3 are balanced [26].

This segmentation technique requires a fine-tuning of their parameters in order to be able to reach the equilibrium condition. It is affected on its performance and sensitivity by the following issues [26]:

- 1) Need for optimization of the parameters;
- 2) Dependence on the initialization of the snake points;
- 3) Dependence on the number of points constituting the snake;

In 2002, Gutierrez et al. [36] proposed an automated technique for carotid IMT measurement based on the model above mentioned. In this approach, active contour vertices could move being subjected to the two energies explained and also to the damping energy. The internal energy was related to the contour curvature, while the external energy was the local magnitude of the image gradient. The damping energy was proportional to the velocity of each contour vertex and in opposite direction. Using different weighting factors to each energy, the three energies were linearly combined.

Comparison between this approach results for 180 images and the respective human measurements found an error of $90.0 \pm 60.0 \mu\text{m}$. The main contribution of this approach was the inclusion of the damping energy, which helped to smooth and stabilize the contour evolution. However, the high error value of the IMT measurement limits its application.

In the same year, Cheng et al. [37] proposed another snake-based approach. The methodology attempted to solve the poor segmentation performance in the region comprised between the intima and the adventitia layers, since both layers have bright features. The figure 3.4 sketches a sample of this erratic behavior, where the noise attracted the snake towards intima, instead of adventitia. To overcome this limitation, the external energy was redefined as follow:

$$E_{ext}(v) = - \int_{\Omega} g_0(|f_M * I| + D * I) ds = - \int_{\Omega} F(v) ds \quad (3.5)$$

where I is the original ultrasound image, f_M represents the Macleod operator and g_0 is the gravity constant. The matrix D is defined as:

$$D = A \begin{bmatrix} 0 & -1 & 0 \\ 0 & 0 & 0 \\ 0 & 1 & 0 \end{bmatrix},$$

where A is a positive weighting factor. This matrix prevents possible trapping of the snake as described before, since its central column is a vertical gradient that has a negative weight upwards and a positive weight downwards.

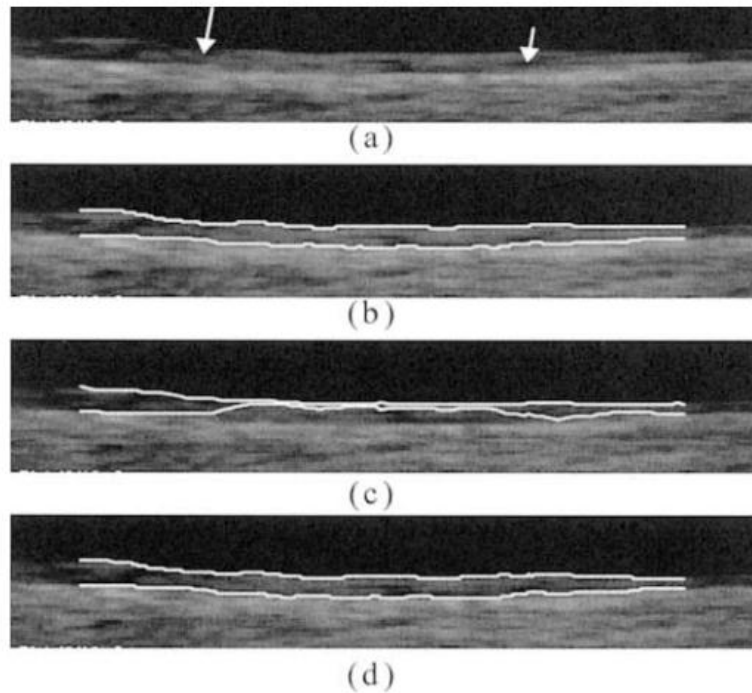


Figure 3.4 - Possible snake erratic behavior in segmenting the LI and MA layers. (a): original image of the far wall. (b): Segmentation of Cheng's snake; (c): erratic behavior of a traditional snake; (d): ground truth obtained by manual segmentations [37].

The authors validated their technique [37] versus human tracings, by computing the mean squared error between them. The performance results were better than the Gutierrez et al. approach but it still had a reasonable error.

In 2007, Loizou et al. [38] addressed the problem of image pre-processing standardization in order to overcome some snake limitations. They observed that most of the CCA segmentation techniques were lacking speckle noise reduction and proposed a preliminary image intensity normalization followed by despeckling. Considering the typical ultrasound image discretized on integers from 0 to 255, the authors proposed to scale image intensities so that the median of the blood was between 0 and 5 and the median of the adventitia layer was between 180 and 190. After this pre-processing step, the optimal snake parameters were $\alpha(s) = 0.6$ and $\beta(s) = 0.4$, while the external force was weighted by a parameter $\gamma(s) = 2$. The technique was tested in 100 images and the IMT measurement error was $50.0 \pm 25.0 \mu\text{m}$ and a manual interaction was still required to place the initial seed points of the snake in the artery lumen.

3.4 LOCAL STATISTICS AND SNAKES

One of the main objectives on the IMT measurement algorithms is to obtain a full automated approach. In 2007, Delsanto et al. [39], [40] proposed a combined technique of local statistics and snake-based segmentation, in order to obtain the automation required. This technique was divided into two distinct parts:

- 1) A module aiming at locating the carotid artery in the image frame, where local statistics were the basis;
- 2) A segmentation and IMT measurement module using a snake-based algorithm.

The carotid artery location was achieved by clustering the image into a bidimensional histogram with each pixel being presented as the mean and the standard deviation values of the image in a 10x10 neighborhood. Since the pixels in the lumen regions are ideally black having a very low mean and standard deviation, it would be possible to automatically detect the lumen points. The figure 3.5 shows the histogram with the black points corresponding to lumen points, which supports this technique fundamentals.

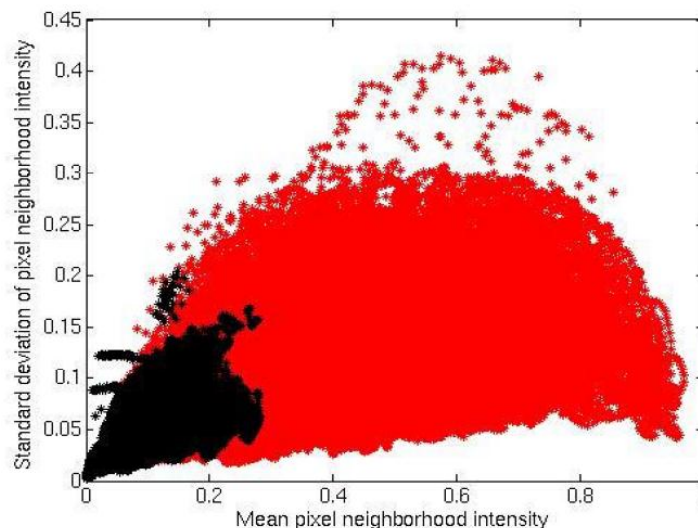


Figure 3.5 - Average value and standard deviation of the pixel neighborhood intensity (normalized values). The pixels belonging to the carotid lumen are depicted in black and it is evident how that pixels are located in the first classes [39].

Based on the intensity profile of each column, the near and far adventitia layers were found. Finally, a snake-based algorithm was applied with the following formulation:

$$E = \int_0^1 \frac{1}{2} \alpha(s) |v'(s)|^2 + \gamma(s) E_{ext}(v(s)) ds, \quad (3.6)$$

with the optimal snake parameters $\alpha(s)$ and $\gamma(s)$ equal to 0.1 and 0.01, respectively. This approach was tested in 63 images and it obtained an IMT measurement error equal to $63.0 \pm 49.1 \mu\text{m}$, comparing with human tracing. This strategy was completely user-independent but authors declared that noise could preclude the CCA localization in about 10% of cases.

In 2008, the same research group proposed a further improvement of the technique [41]. The CCA location was identical to previous version, and once detected, a fuzzy K-means classifier was inserted in the segmentation module in order to cluster the pixels inside the ROI. Three possible clusters were considered: (a) lumen; (b) intima and media layers and (c) adventitia layer. The border between (a) and (b) was considered as the initial guess of the LI boundary while the border between (b) and (c) was considered as the MA interface. Then, using the same snakes formulation, the contours were refined and its performance was evaluated in 45 images – the IMT measurement error was reduced to $35.0 \pm 32.0 \mu\text{m}$ and only 8% of the images could not be automatically processed.

In 2009, Molinari et al. [42] proved that the referred segmentation [39], [41] performance was independent on the scanner used and the last version of this implementation showed an IMT measurement error of $10.0 \pm 10.0 \mu\text{m}$, when tested in 200 ultrasound images. The figure 3.6 reports a sample of completely user-independent segmentation of the near and far wall carotid wall obtained using this approach.

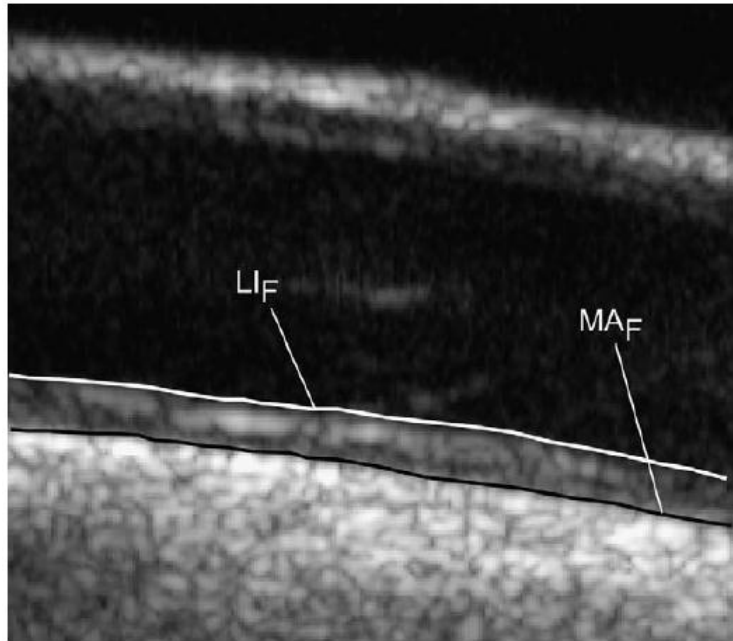


Figure 3.6 - Completely user-independent segmentation of the near and far carotid wall by a technique proposed by Molinari et al. [41]

3.5 NAKAGAMI MODELING

Destremes et al. [43] proposed a segmentation approach based on the Nakagami mixture modeling and stochastic optimization. They proposed the intensity modelling of a small ROI image to segment the carotid, assuming that if a ROI window contained the carotid wall, then the intensity was characterized by a specific pattern and the presence of speckle noise.

They considered several small ROIs and analyzed the signal, as sketched in the figure 3.7. The vertical profiles were analyzed considering three assumptions:

- 1) The lumen corresponded locally to the distribution with lower mean;
- 2) The intima-media complex corresponded locally to the mixture;
- 3) The adventitia corresponded locally to the distribution with higher mean.

The right panel of the figure 3.7 shows the assignment of the four different profiles to the 3 regions. In a first step, they computed the maximum *a posteriori* estimator of the proposed model, using the expectation maximization algorithm. The optimal segmentation was achieved using a variant of the exploration/selection algorithm, and the convergence was assured asymptotically and independent from the initial solution.

This technique proved to have very high performance rates in CCA segmentation. However, the assumption 3) limits its application in processing a generic pathology image, since that in presence of calcified plaque, the adventitia might not present the local distribution with higher mean value.

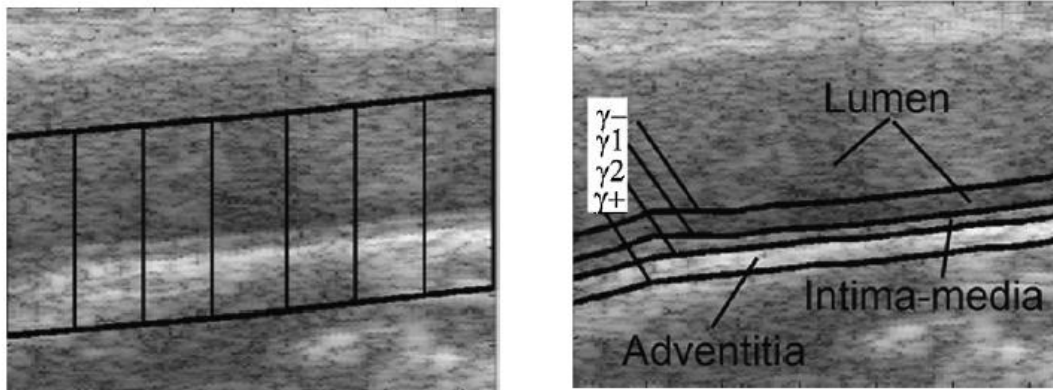


Figure 3.7 - Right panel: representation of the ROIs selected in dynamic processing strategies. Each ROI contains the lumen, the intima-media structure and the adventitia layer. Left panel: assignment of the four boundaries [43].

3.6 HOUGH TRANSFORM

Between 2004 and 2009, Golemanti et al. [44] developed a segmentation algorithm based on the Hough transform. They assumed that the CCA layers are straight in longitudinal projections and circular in transverse projections, thus being suitable to use the mentioned transform, which is normally used to detect lines and circles. The dominant lines in longitudinal images represent the LI and MA boundaries and the distance between them was taken as the IMT measurement.

This technique is divided in two phases: 1) Carotid artery wall representation and 2) Intima-media thickness representation. The workflow of both phases is presented in the figure 3.8.

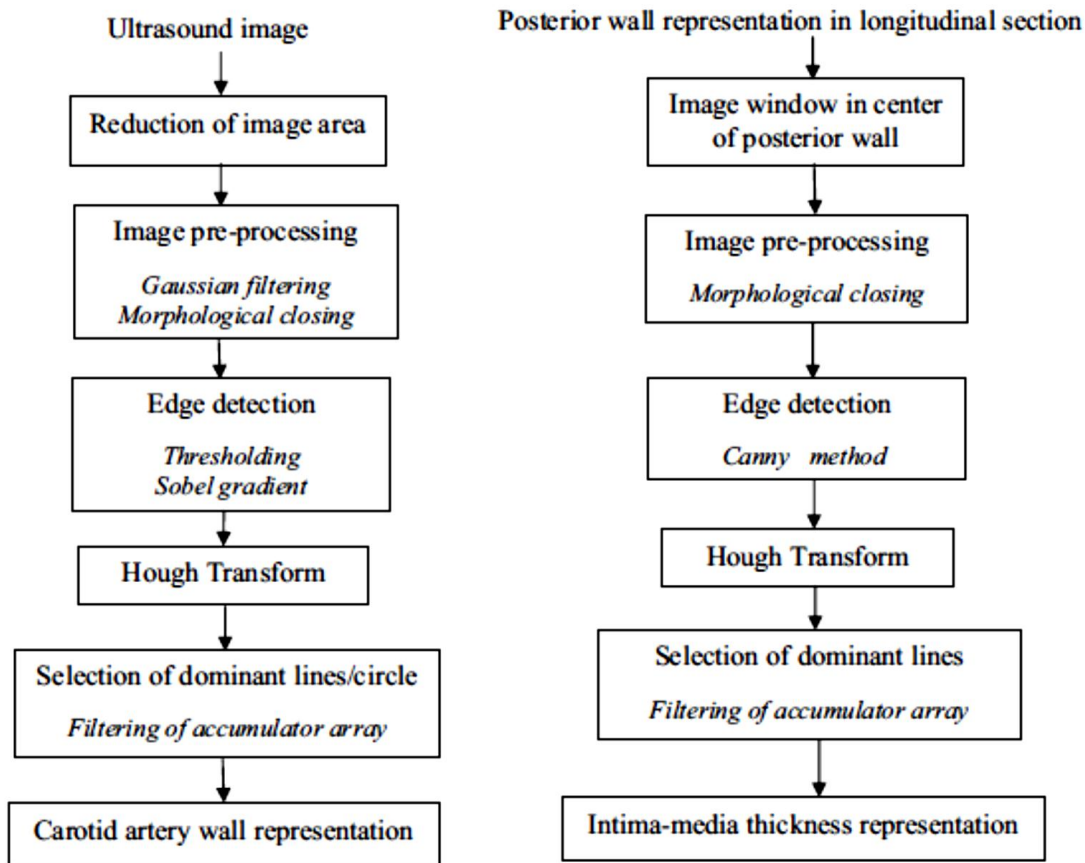


Figure 3.8 - Flow chart of the procedure for (left) the identification of the arterial wall (in longitudinal and transverse sections) and the (right) estimation of the IMT [45].

This approach was shown to be helpful in images with small wall plaques but it was highly dependent on a straight and horizontal vessel in the image to achieve a good performance. Validation was done against human tracings and the sensitivity was 96% and 82% in longitudinal and transverse projections, respectively, while specificity was 96% in both the projections.

3.7 INTEGRATED APPROACH

In 2009, Molinari et al. [42] developed an architecture for vessel wall segmentation, which consisted of two phases:

- 1) A module for the automatic location of the CCA in the image;
- 2) A segmentation procedure that automatically traces the LI and the MA contours of the far wall once CCA was located.

In phase 1, the local intensity maxima of each column are processed to detect both CCA walls. These points are called seed points and a procedure is

then applied to remove short or false line segments and to join close and aligned segments. Once CCA has been detected, the phase 2 of the algorithm begins and the image is scanned: the intensity profile of each column was processed by using a fuzzy K-means classifier that assigned the pixels to three clusters: 1: lumen; 2: intima and media layers and 3: adventitia layer.

This algorithm has the advantage of being completely user-independent but the IMT measurement error (tested in 200 images) was higher than most of previously cited techniques ($54.0 \pm 35.0 \mu\text{m}$).

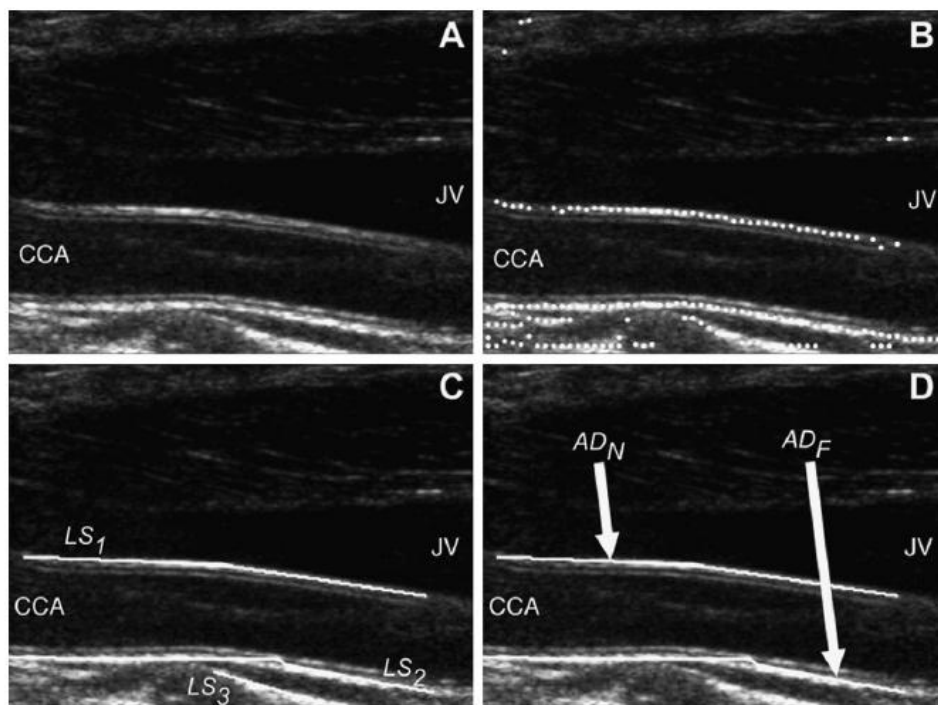


Figure 3.9 - Representation of the integrated approach by Molinari et al. A: original image of the CCA. B: Seed points detected; C: Line segments obtained by connecting the seed points and discarding fragmented and misplaced lines. D: Final segmentation results [42].

4 MATERIALS AND METHODS

This chapter includes the description on acquisition of data and its organization, the methodology of the segmentation algorithm from the pre-processing to the segmentation approach itself, and then, the Graphical User Interface implemented in order to use the proposed methodology.

4.1 ACQUISITION OF DATA

In order to create and evaluate the algorithm suggested in the present chapter, ultrasound images of the CCA were acquired by an expert. All the images were recorded using a *GE Logiq e Portable Ultrasound System* [46] which allows to measure the IMT after the image acquisition, in order to provide a ground-truth for the IMT.

To obtain a good contrast between the vessel wall and the lumen, the ultrasound beam should be aimed perpendicular to the vessel. Figure 4.1 shows two typical images of the CCA: image A has a visible intima-layer both along the near and far wall, while in the image B the intima-layer is only visible for a small section along the far vessel wall, and there is also more noise in the lumen area. In order to provide a clear explanation of the algorithm implemented, the image A is used as the main example throughout this chapter and the effect of every algorithm step will be displayed over the referred image.

The images acquired are stored with the RGB color model.

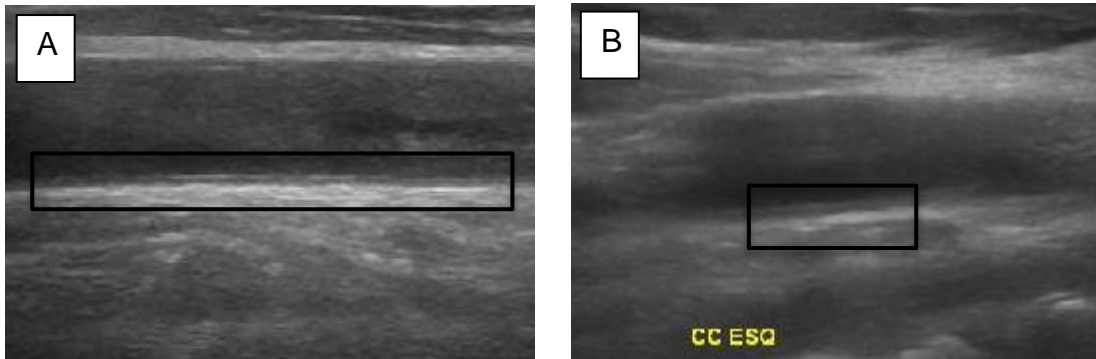


Figure 4.1 – Typical images of the CCA. The image A presents a well-defined far wall along all the image, while the image B presents a good definition of the far wall only in the center of the image.

4.2 METHODOLOGY

In this section, the segmentation algorithm implemented is explained and each phase of the methodology is detailed with images displaying the results of every step applied. The purpose of the implemented segmentation is to classify the analyzed carotid artery as healthy or unhealthy, depending on the thickness of its wall, in order to report the risk of atherosclerosis or to control its growth.

A typical image processing and classification problem involves a pre-processing step, segmentation techniques, features extraction and a final classification. The figure 4.1 summarizes the workflow of the segmentation.

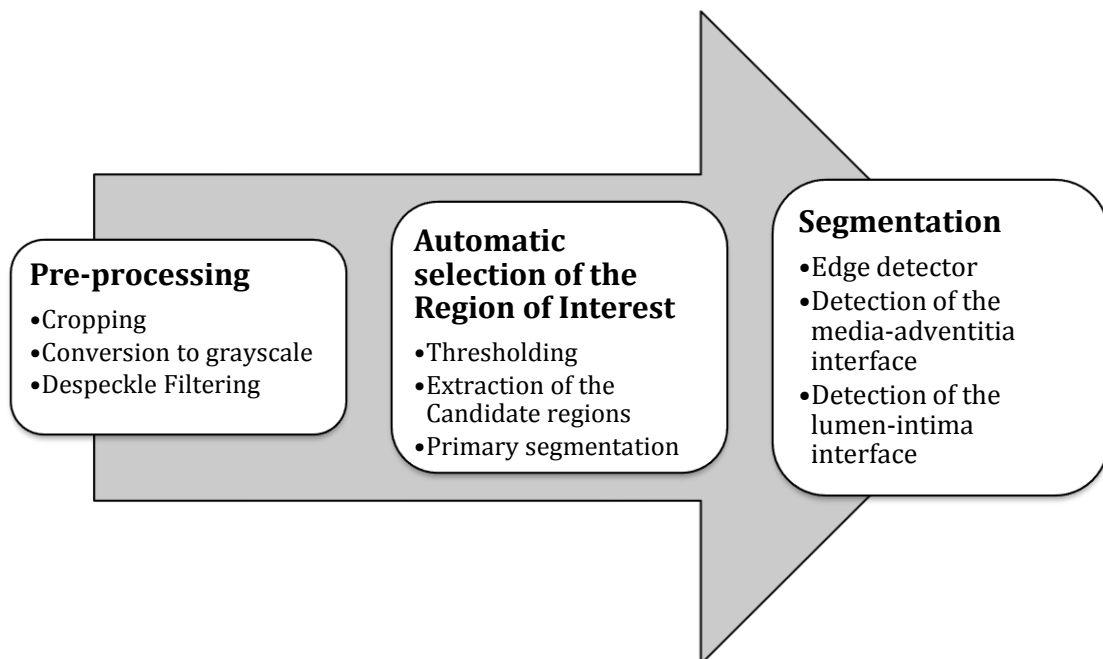


Figure 4.2 – Workflow of the segmentation.

4.2.1 PRE-PROCESSING

The echography image is first subjected to a pre-processing step before its characterization. This is a very important step in order to get a “clean” version of the original echography image and it is a huge progress towards an efficient segmentation and a good performance.

CROPPING

The DICOM [47] echography image serves as the input of the algorithm and the first pre-processing step is the cropping. The cropping was implemented in order to remove the black borders surrounding the image. This process is sketched in the algorithm 1 and it searches through the columns near each border (left, right, top and bottom) until it finds the first pixel with intensity 0 (phase 1). Then, it continues searching until it finds a pixel with intensity different from 0 and the location of the found pixel is used to crop the image in the respective border (phase 2). A variable is used to control what is the current phase. The coordinates of the 4 resultant pixels (left, right, top and bottom) are used to define the region of the image to maintain, cropping all the remaining.

Algorithm 1: Cropping example for top border

```
control = 0;
for each line of the image
  if control = 0;
    Phase 1
    if pixel intensity equals 0
      control = 1;
    end
  else
    Phase 2
    if pixel intensity differs from 0
      crop = line number;
    end
  end
end
```

Some files have additional information, namely the patient identification and the acquisition configurations. The used technique takes this possibility into account and achieves the objective also for that kind of images. The figure 4.3 represents the 2 types of possible images (with and without the patient information) and the respective crop implemented.

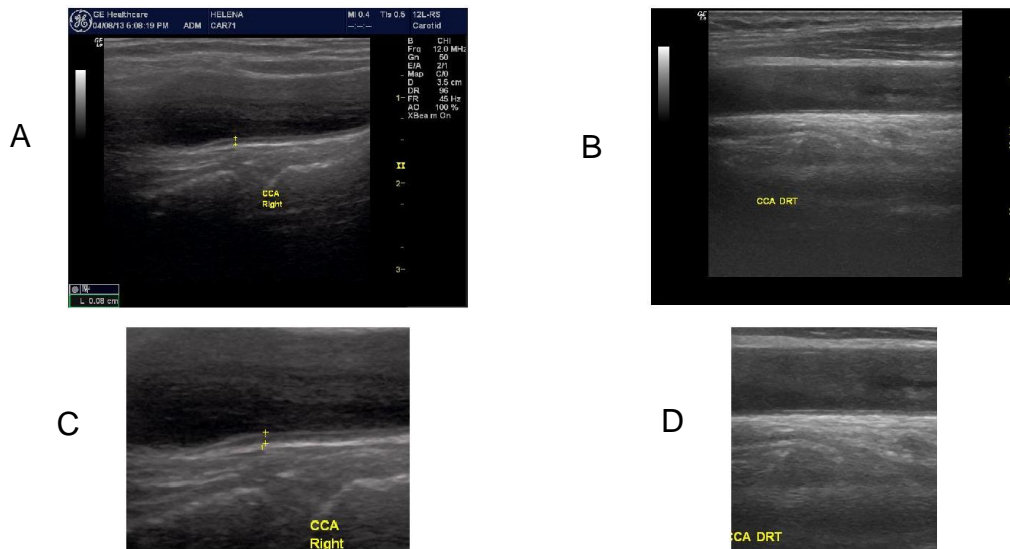


Figure 4.3 – Border cropping of the images used. A: Original image with patient information and crop (C). B: Original image without patient information and crop (D).

FILTERING

Due to the presence of speckle noise in the ultrasound image, the filtering is an important step before the segmentation approach. Thus the image is first converted into grayscale and a median filter is applied, using a 7x7 moving window, as described by Loizou e al. [17].

The filtering reduces the noise while smoothing the edges of the image. As presented in the figure 4.4, the different regions of the image become more homogeneous and easier to segment, due to the effect of the median filter.

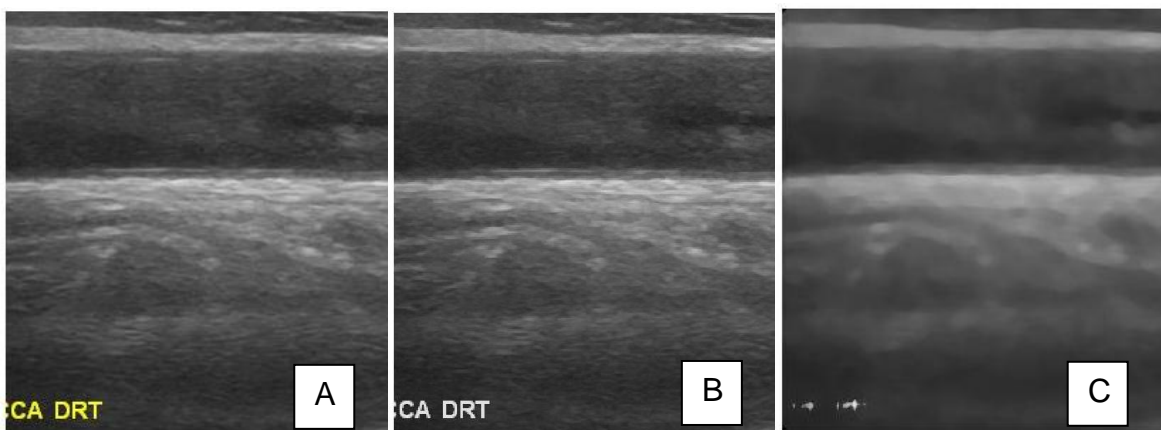


Figure 4.4 - Image filtering. A: Original image; B: Conversion to grayscale; C: Median filtering [7x7].

4.2.2 AUTOMATIC SELECTION OF THE REGION OF INTEREST

As mentioned in section 2.2.2., the Manheim Carotid Intima-media Thickness Consensus [19], has defined the IMT as the distance between the

two parallel echogenic lines (correspondent to the bright pixels) present in ultrasound images on the far wall of the carotid artery, as shown in figure 4.5. After the pre-processing, the biggest challenge is to define the region to segment. The procedure to find the region of interest (ROI) encompasses thresholding and extraction of two candidate regions. The correct region is then chosen in the last phase of the algorithm. In addition, a primary segmentation is accomplished in order to improve the algorithm performance and time-dependency.

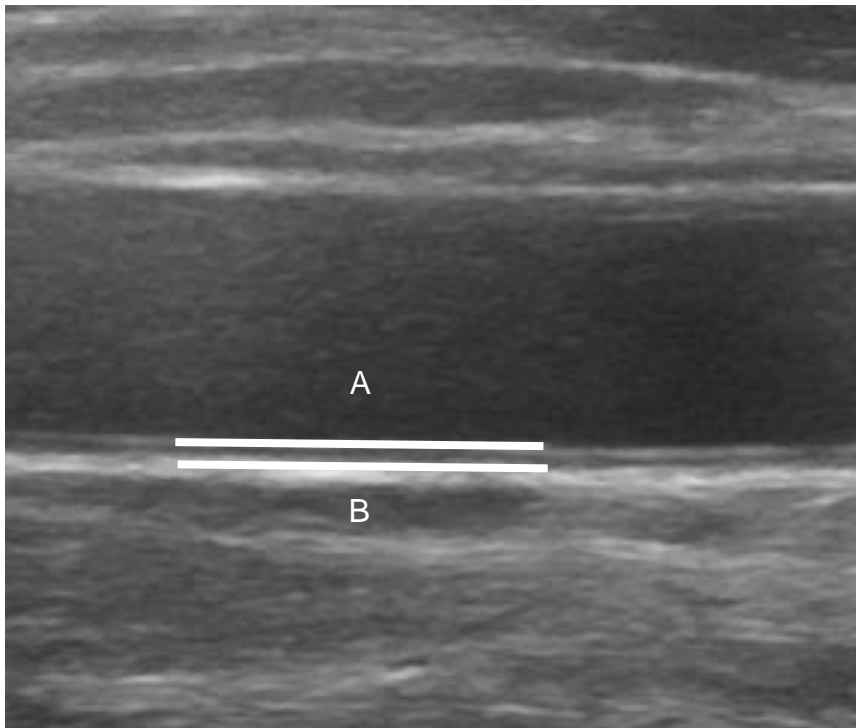


Figure 4.5 - Double line pattern characteristic of the ultrasound carotid images. A: Lumen-intima interface; B: Media-adventitia interface.

THRESHOLDING

With the purpose of solving this problem, first an algorithm was implemented to search the lumen, which is characterized by the darker pixels in the image. Since that task is not complex, a simple thresholding method was applied, that replaces each pixel in an image with a black or white pixel, according to the threshold: if the pixel intensity is lower than the threshold value, it is replaced as a black pixel, otherwise a white pixel is considered, like illustrated by the algorithm 2.

Algorithm 2: Thresholding

```
// f(x,y): Image  
if f(x,y) < threshold  
    f(x,y) = 0;  
else  
    f(x,y) = 1;
```

The threshold used is equal to the intensity level corresponding to the first pixel that comes in the histogram after the cumulated frequency has reached 60% [27]. This value defines the pixels corresponding to the blood turbulence in the lumen [27].

As can be seen in the histogram of the figure 4.6, the threshold value (represented with the vertical line labeled “Threshold”) cover the pixels with lower intensity, while preserving the brighter pixels. Subsequently, the pixels belonging to the lower intensity group (labeled as A in figure 4.6) are set as black pixels and the remaining (labeled as B in figure 4.6) are set as white pixels, resulting a binary image.

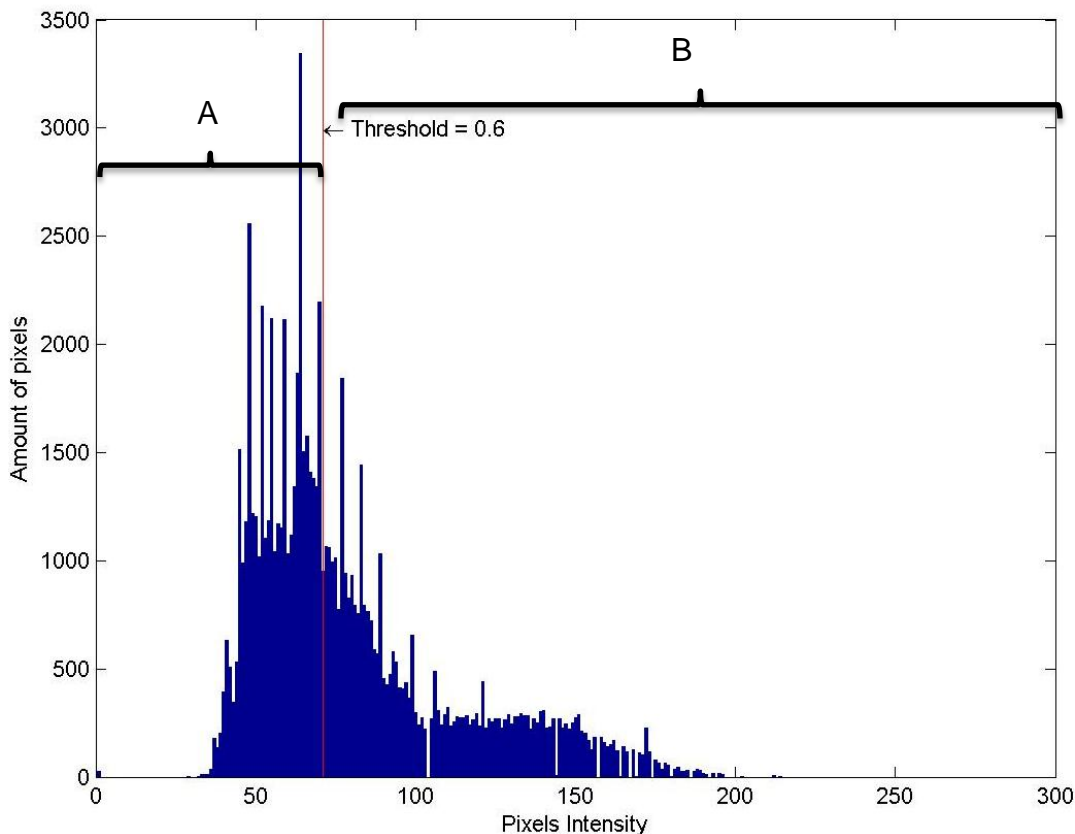


Figure 4.6 – Intensity histogram of the image used as the main example.

In figure 4.7, it is possible to identify a well-defined group of black pixels in the region of the lumen (labeled as A). However, another similar region appears in the bottom (labeled as B) of the image, which can affect the correct

selection of the ROI. For this reason, in the next step, two regions of interest will be chosen and the correct one will be determined after the segmentation, according to the results obtained.

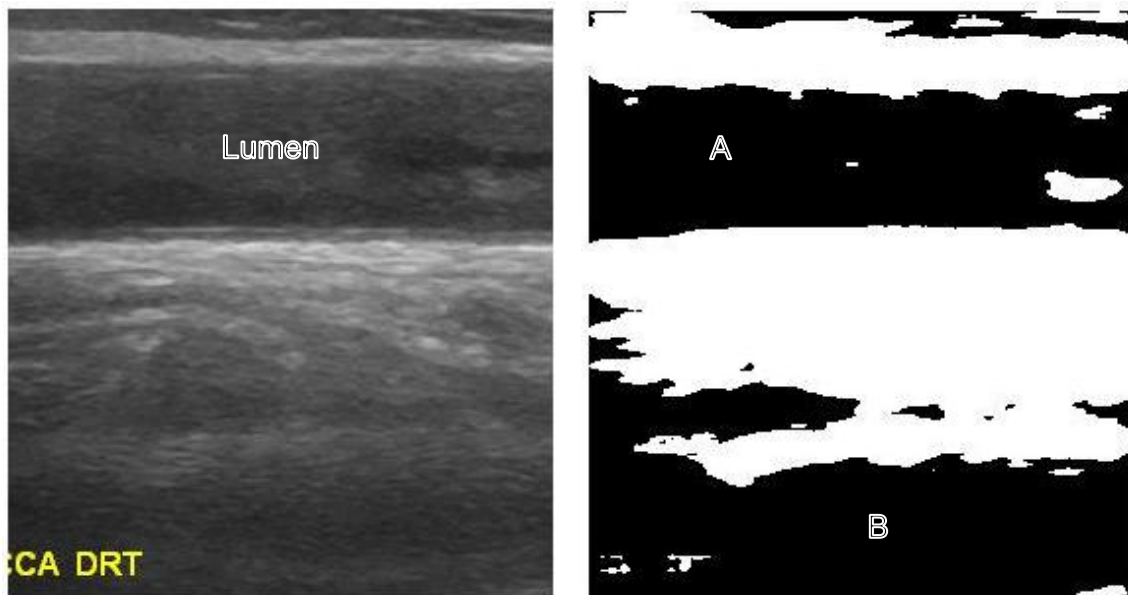


Figure 4.7 - Result of the thresholding method over the image used.

EXTRACTION OF THE CANDIDATE REGIONS

Once the binary image is obtained, a connected-component analysis is done to detect connected region in binary images and, in this case, the algorithm finds and defines the regions containing black pixels, since the objective is to recognize the lumen area in the image. The connected-component analysis searches in all pixels of the image and, when it finds a black pixel, the algorithm starts a search in the pixels of the surroundings. If it discovers a black pixel in the surrounding, the process is repeated until the last matching pixel is discovered.

The described analysis provides a list of all the connected black pixels, which permits to calculate the area of the regions composed by them. As presented in figure 4.7, the thresholding create two main regions with black pixels. Thus, two candidate regions are considered and they correspond to the two regions with larger area (labeled in figure 4.7 as A and B), from the obtained with the connected-component analysis. A rectangular bounding box including the referred regions is defined and result is presented in the figure 4.8. If just one region is possible to define, that region is used as the only input for the rest of the methodology.

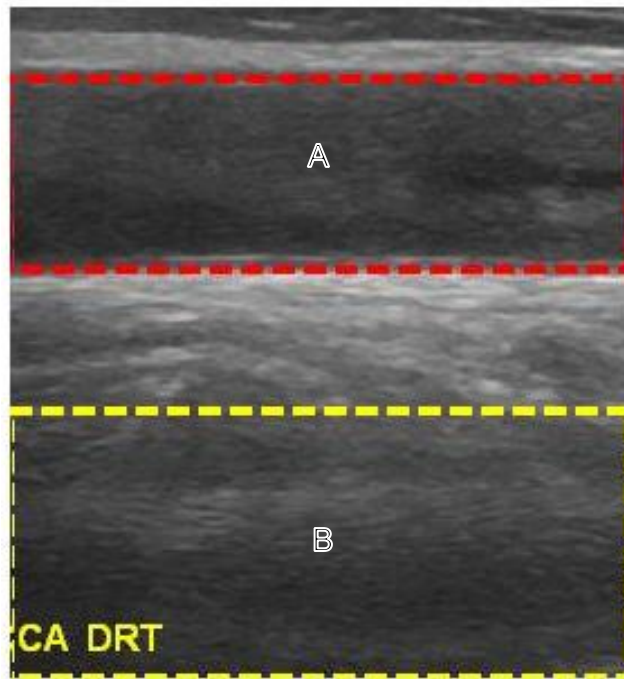


Figure 4.8 - Candidate regions found with the technique applied.

PRIMARY SEGMENTATION

The segmentation based on the processing of the intensity profiles demands a huge computational cost, since the algorithm has to search all pixels of all the profiles. In order to reduce the computational cost, consequently reducing the time necessary for segmentation, and to improve the algorithm performance, a first approach of segmentation is done at a coarse scale.

As described in 4.1, the acquisition of the images should be done with the ultrasound beam aimed perpendicular to the vessel. If the acquisition is not perfectly done, some regions of the carotid artery may not be well defined, as shown in image B of the figure 4.1. In order to prepare the algorithm for these distorted areas, the bounding boxes previously obtained are divided in three sub-regions with the same size (as shown in figure 4.9). Thus, the ROI is segmented in three different parts and the low quality areas will not influence the segmentation results of the remaining. The division in three areas permits to analyze separately the left and right side of the image, as well as the central region, ensuring the desired result.

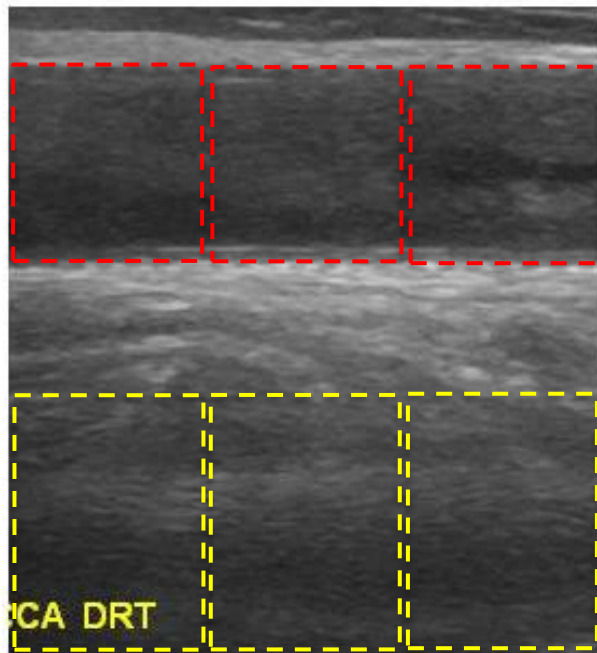


Figure 4.9 – Division of each bounding boxes in three with same size.

The segmentation of the CCA should be carried out preferably in the far wall, as recommended by the Mannheim Carotid Intima-media Thickness Consensus [19]. Although, the automatic ROI selection previously done had as objective the location of the lumen instead of the far wall. It is known that the far wall, in an echography, can be found below the lumen. Thus, the candidate regions are redefined to include the required area, as depicted in figure 4.10.

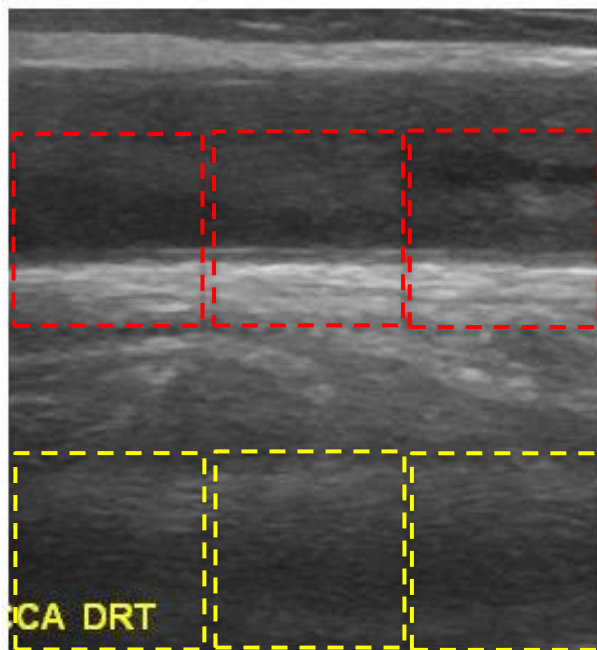


Figure 4.10 – Redefinition of the sub-regions in order to include the far wall of the carotid artery.

Once the regions of interest definition is completed, the result are 6 different regions to segment. A thresholding is applied to each one of the six images as described before in 4.2.2, in order to separate the far wall from the background. The binary images resultant of the thresholding are presented in the image A of the figure 4.11.

A connected-component analysis of the binary images is applied as previously described. However, instead of analyzing the connectivity of the black pixels, in this case the analysis aimed the white pixels, since they constitute the far wall. Then, only the larger connected area of each image was preserved, corresponding to the far wall of the carotid artery, as shown in the image B of the figure 4.11.

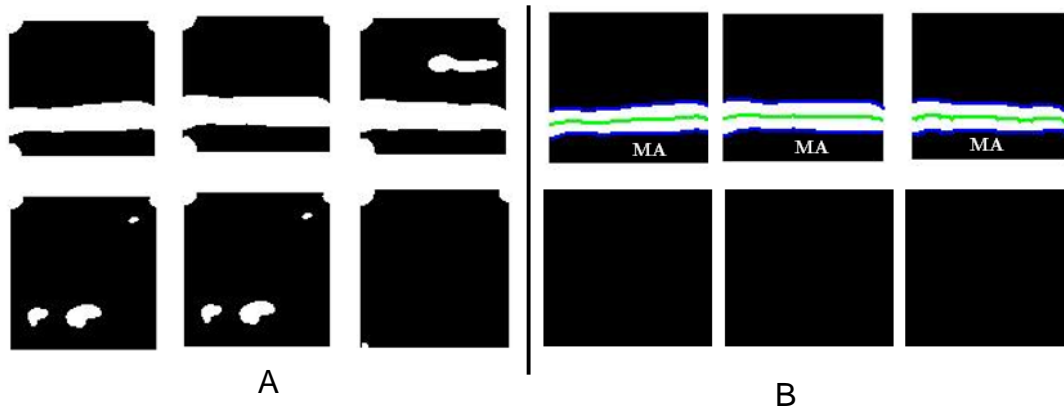


Figure 4.11 - Initial segmentation. A: Result of the thresholding method applied in each sub-region. B: Segmentation of the biggest object in the image.

After that processing step, the contours of the white objects present in each image were defined using the following algorithm:

```

Algorithm 3: Primary segmentation
// g(x,y): Region of interest
for a = each column in the image
  for b = each row in the image in ascendant order
    if g(a,b) = 1
      uppercontour = [uppercontour; a, b];
      break;
    end
  end
  for b = each row in the image in descendent order
    if g(a,b) = 1
      lowercontour = [lowercontour; a, b];
      break;
    end
  end
end

```

The line concerning the lower contour (identified in the image 4.11 as MA) is used as input in the next step of the algorithm, in order to facilitate and

enhance the segmentation, as it provides a first guess of the points. This line will be called “first contour” throughout the explanation of the algorithm.

4.2.3 SEGMENTATION

The final segmentation consists of the improvement of the first contour previously obtained. With this objective, the filtered image shown in figure 4.5 is convolved with the first-order derivative of the Gaussian function. This step works as an edge detection and is followed by the search of local maxima in the neighborhood of the previously found segmentation.

In the image processing, a Gaussian blur is the result of convolving the image with a Gaussian function. In two-dimension, the Gaussian function is defined by:

$$g(x, \sigma) = \frac{1}{2\pi\sigma^2} e^{-\left(\frac{x^2+y^2}{2\sigma^2}\right)}, \quad (4.1)$$

where σ is the standard deviation of the Gaussian distribution from the center point. It is widely used to reduce image noise and it has also been used in computer vision in order to enhance image structures.

The derivatives of the Gaussian function are also an important tool in image segmentation. The first-order derivative in two-dimensions is defined by:

$$g'(x, y, \sigma) = -\frac{x}{\sigma^2} \frac{1}{\sigma\sqrt{2\pi}} e^{-\left(\frac{x^2+y^2}{2\sigma^2}\right)} \quad (4.2)$$

When convolved with an image, the formula 4.2 produces a surface, which contours are defined by a Gaussian distribution. This process permits the arising of the lumen-intima and adventitia-media interfaces as the center point of a Gaussian function, as proved in the image C of the figure 4.16. This transformation facilitates the segmentation of the IM complex by searching absolute maxima near the neighborhood of the first contour previously obtained, once that the maxima are well defined.

Thus, the image gradient is computed using the aforementioned first-order Gaussian derivative. The convolution of this gradient with the carotid echography after pre-processing (denominated $f(x,y)$) is computed according to the following equation:

$$h(x, y) = f(x, y) \otimes g'(x, y, \sigma) \quad (4.3)$$

The differences in the intensity profile produced by the filtering and the Gaussian derivative are displayed in figure 4.12. It is possible to confirm that the filtering softens the contours (image B) of the carotid, while the first-order derivative of the Gaussian function highlights the edges (image C). The graphs are correspondent to the intensity profile in the column, identified by the dashed line in each image.

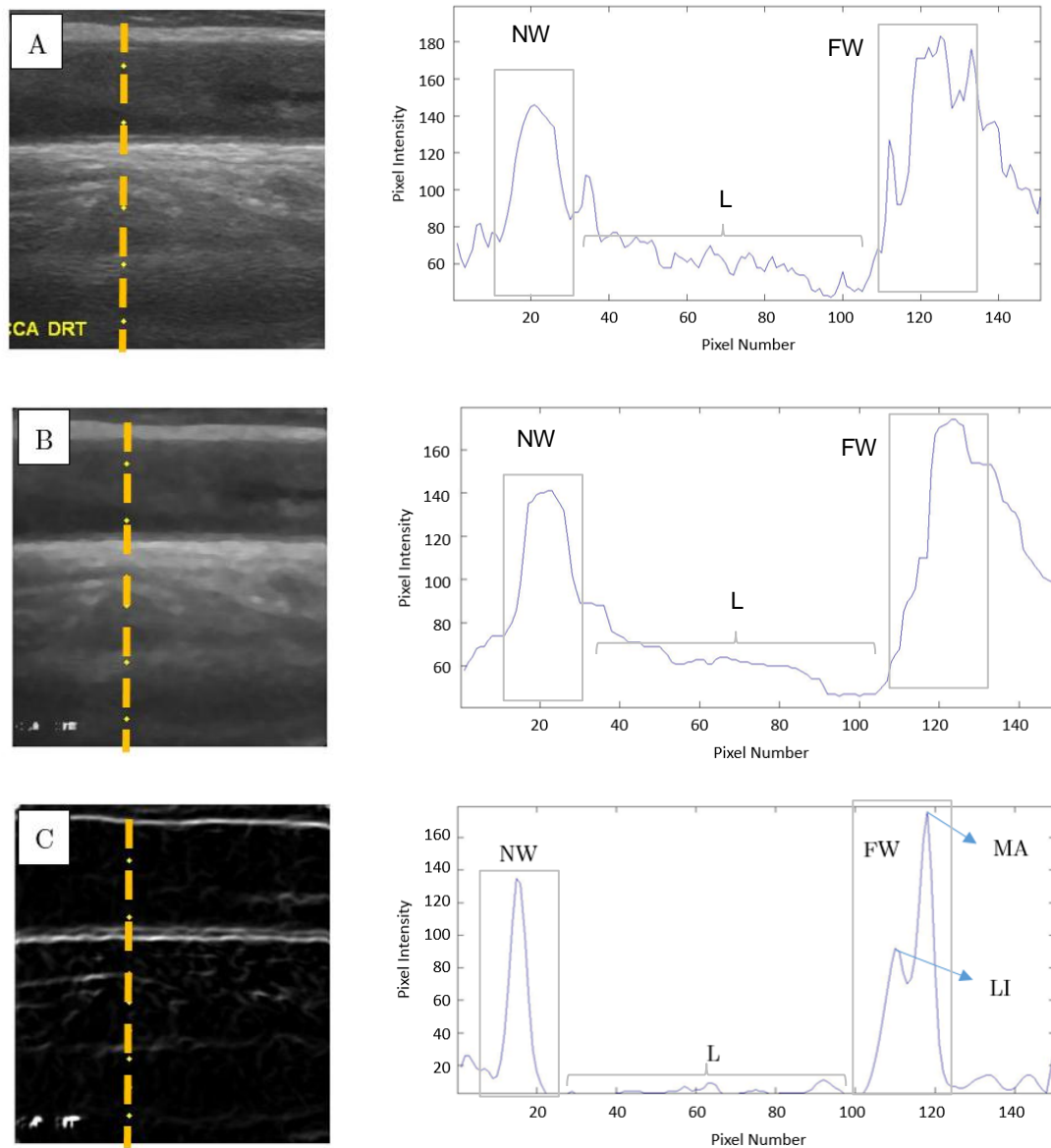


Figure 4.12 - Results of the filtering (B) and the first-order derivative of the Gaussian function (C) in the processed image (A) and in its intensity profiles. The intensity profiles are correspondent to the column represented by the dashed line in each image. NW: Near Wall; FW: Far Wall; L: Lumen; MA: Media-adventitia interface; LI: Lumen-intima interface.

In the figure 4.12, the image A is before the pre-processing and the respective graph displays a set of points with low intensity (labeled as L)

between two sets with high intensity pixels (labeled as NW and FW), as expected. However, the lumen-intima (LI) and media-adventitia (MA) interfaces in the far wall (FW) are not sufficiently defined, mostly in the media-adventitia since there are several local maxima instead of a single maximum. This fact avoid the distinction between the correct peak and different peaks provoked by the interferences in the acquisition.

The image B in the figure 4.12 is after the pre-processing, which includes a median filtering. Comparing to graph A, the graph B presents a smoother profile, with preserving the edges. Although, it is still difficult to distinguish the intima-media complex in the far wall. Hence, the first-order Gaussian derivate has a crucial importance, since it is able to highlight to lumen-intima and media-adventitia interfaces.

The image C in the figure 4.12 displays the image after the convolution of the image B with the first-order Gaussian derivative. The intensity profile presented in graph C shows two well defined Gaussian distribution in the far wall (FW), with the center points corresponding to the interfaces of the lumen-intima and media-adventitia, identified in graph C as LI and MA.

DETECTION OF THE MEDIA-ADVENTITIA INTERFACE

The intensity profile of each column of the image is processed using the first contour results obtained in 4.3 as follows:

- 1) Searching for absolute intensity maxima near the neighborhood of the first contour points. The neighborhood is defined by the pixels whose distance between itself and the correspondent first contour point is smaller than 0.05 cm. This value is based in the Manheim Carotid Intima-Media Thickness Consensus [19], which defines plaque as a focal structure encroaching the arterial lumen of at least 0.05 cm.
- 2) If a maximum cannot be found in the defined conditions, the column is rejected and the search continues through the remaining columns. After processing all points of the image, a linear regression is applied to the maxima obtained and the resulting line defines the media-adventitia layer.

The algorithm implemented in this step is presented below:

Algorithm 4: Detection of the media-adventitia interface

```
// fc(y): first-contour position in the column y
// MA(y): media-adventitia contour in the column y
// K: cm to pixel conversion constant

for each column i of the image
  range = [fc(i)-0.05*K, fc(i)+0.05*K];
  maximum = position of the pixel with the absolute intensity maximum in the defined range;
  if maximum is not possible to find
    continue through remaining columns;
  else
    add position of the pixel to MA(i);
  end
end
end
```

DETECTION OF THE LUMEN-INTIMA INTERFACE

Using the media-adventitia interface defined, the intensity profiles are subjected to a new search. In addition to the mentioned Mannheim Carotid Intima-Media Thickness Consensus, a previous study demonstrated that the mean value for the IMT for people with at least 60 years old is 0.79 cm. According to those values, the search is carried out only in the pixels which are between 0.02 and 0.13 cm away from the MA interface. The value of 0.02 cm is smaller than the 0.05 cm used in the detection of the MA interface in order to minimize possible errors in the segmentation of the MA. The value of 0.13 was chosen to cover cases in which the atheromatous plaque has reached a critical thickness, as referred in the work of Belem et al [48]. The search is carried out as follows:

- 1) Searching for absolute intensity maxima near the neighborhood of the MA interface.
- 2) If a maximum cannot be found in the defined conditions, the column is rejected and the search continues through the remaining columns. After processing all points of the image, a polynomial regression is applied to the maxima obtained and the resulting line defines the lumen-intima layer. The polynomial regression was preferred in this case since the atherosclerotic plaque can present a non-linear contour.

The algorithm implemented in this step is presented below:

Algorithm 5: Detection of the lumen-intima interface

```
// MA(y): media-advantitia contour in the column y
// LI(y): lumen-intima contour in the column y
// K: cm to pixel conversion constant

for each column i of the image
  range = [MA(i)-0.02*K, MA(i)+0.13*K];
  maximum = position of the pixel with the absolute intensity maximum in the defined range;
  if maximum is not possible to find
    continue through remaining columns;
  else
    add position of the pixel to LI(i);
  end
end
end
```

The results of the detection of the two interface are illustrated in the figure 4.13. The images 1A, 1B and 1C refer to the segmentation of a single column while the images 2A, 2B and 2C refer to the complete segmentation for each division of the ROI.

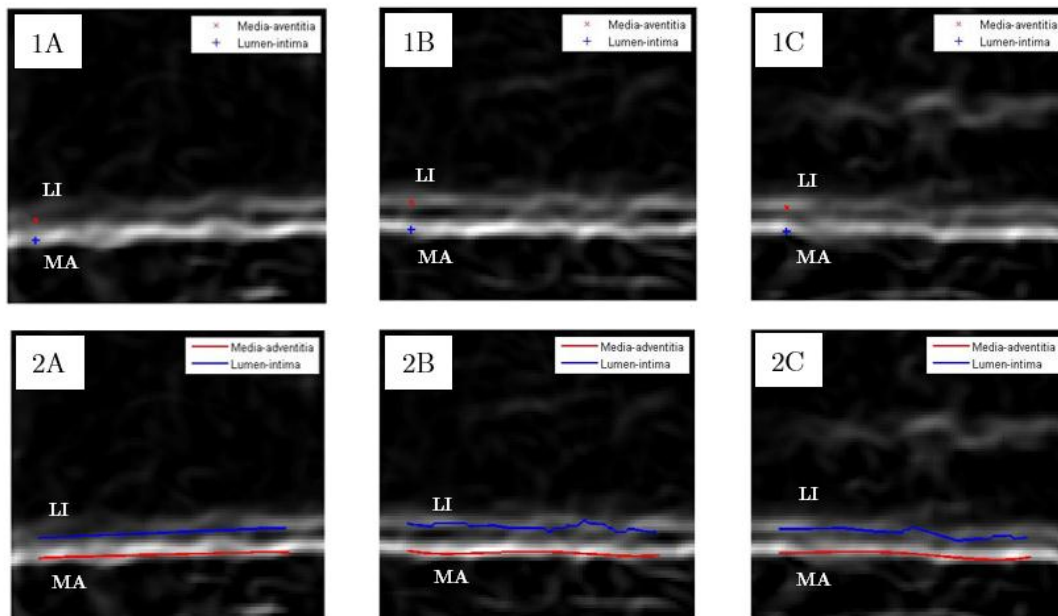


Figure 4.13 – Segmentation of the three sub-regions of the region of interest.

After processing all the points of the image, a polynomial regression of degree 3 [32], [49] is applied to the points obtained and the result is displayed in the figure. The polynomial regression was preferred in this case since the atherosclerotic plaque can present a non-linear contour.

SEGMENTED IMAGE

As mentioned in 4.2.2, the division of the region of interest in 3 sub-regions precludes the influence of distorted areas in the segmentation of well-

defined areas. Thus, it is necessary to choose the best segmentation result from the different 3 obtained.

Since the detection of the two interfaces (lumen-intima and media-adventitia) admit that some intensity profiles may be discarded, it is possible that some of the sub-regions provide a more reliable segmentation than others.

Knowing the aforementioned, the number of intensity profiles used in each segmentation is analyzed. Thus, the sub-region which performs the segmentation using the highest number of intensity profiles is selected as the best approach. On the other hand, all the segmentations using less than 20% of the intensity profiles of the respective sub-region are discarded and its result is not presented.

The figure 4.14 displays the result for each one of the sub-regions. The sub-region A does not meet the minimum requirements and its segmentation is not presented. In contrast, the sub-regions B and C used, respectively, 70% and 50% of the intensity profiles. Consequently, the segmentation with better result was acquired in the sub-region B.

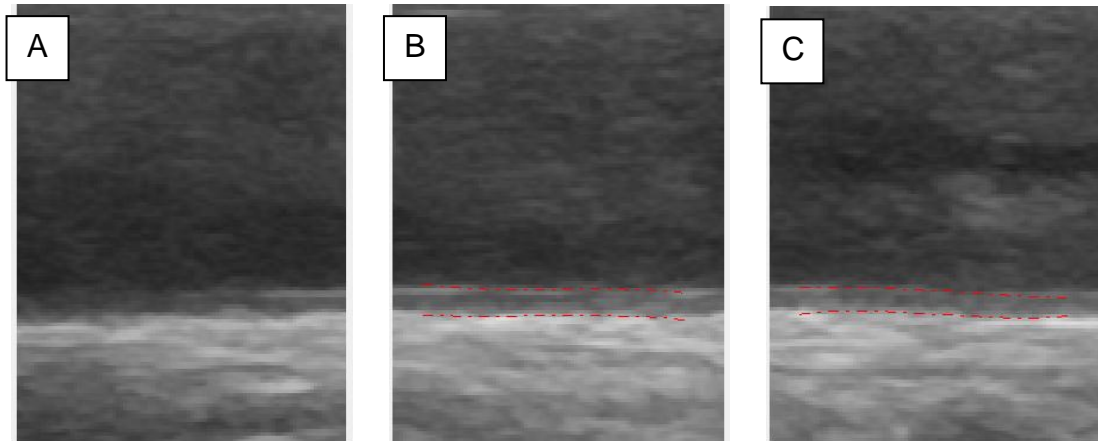


Figure 4.14 - Full Segmentation. A, B, C: sub-regions of the ROI.

4.3 GRAPHICAL USER INTERFACE (GUI)

In order to provide a user friendly environment to analyze an image, a Graphical User Interface was created using MATLAB [50] to be used with the

echography images provided. The figure 4.15 shows the interface appearance and its features are explained below.

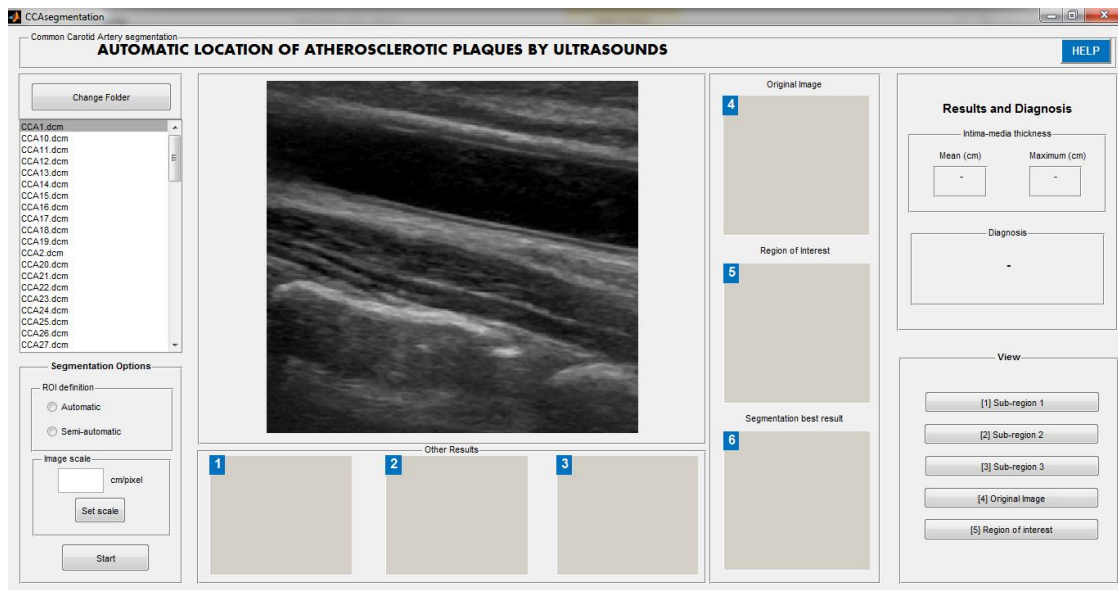


Figure 4.15 - Graphical User Interface implemented with the objective to facilitate the echography images processing.

On the left side (see figure 4.16), the GUI is composed by a list of the files available in the selected folder (labeled as A) that can be changed; images can be displayed by clicking in the list. Once the image is selected, the ROI selection method (labeled as B) should be selected and the push button “Start” (labeled D) starts the process of segmentation. The scale of the image used to compute the IMT can be changed in the section labeled C, according to Appendix C.

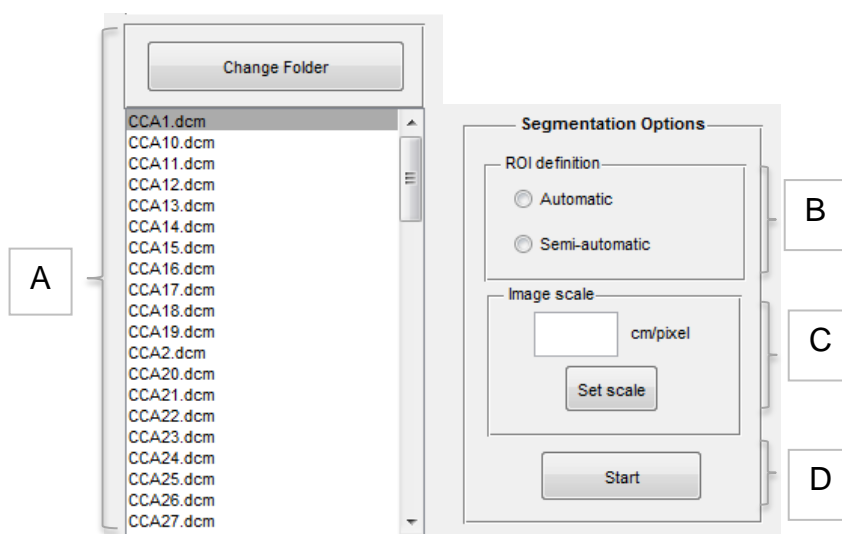


Figure 4.16 - The push button "Change Folder" allows to select the folder containing the images to process. It is set by default to the folder containing the echographies used in this work. The segmentation can be done following 2 different methods: Automatic and Semi-automatic (B) – after the option is selected, the push button “Start” starts the segmentation (D).

The results are displayed as shown in figure 4.17. The images labeled with numbers (1 to 6) can be seen using the panel on the right of the interface and the value of the mean and maximum IMT is also presented (see figure 4.18). This value permits to classify the carotid artery as healthy or unhealthy, based on the value predefined for each classification.

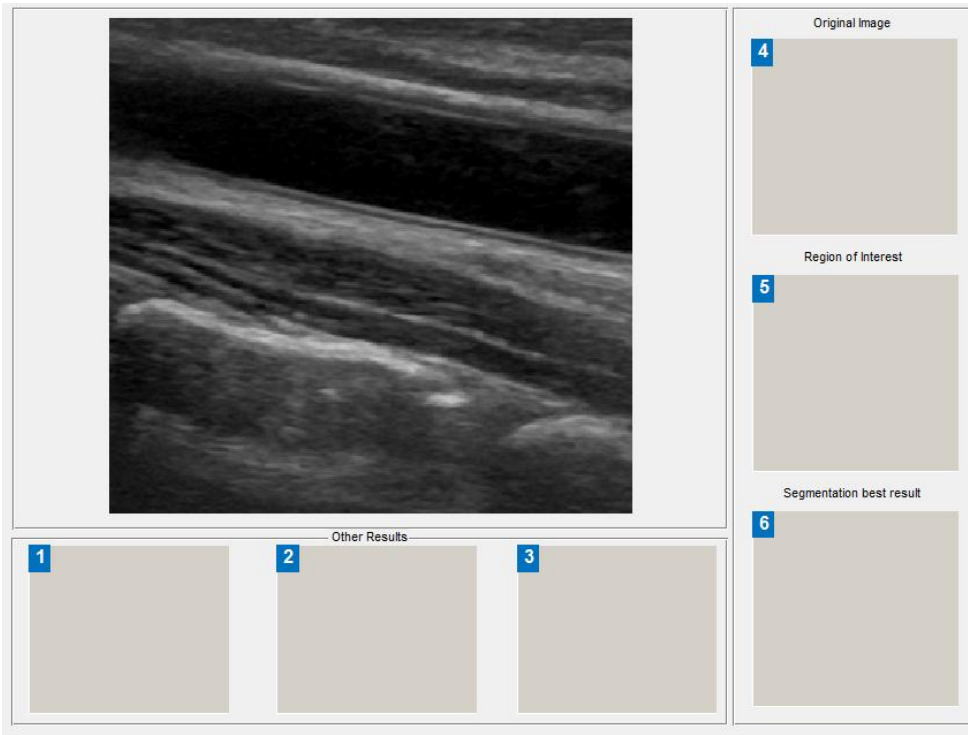


Figure 4.17 – Results display in the GUI. 1-3: Segmentation result for each sub-region; 4 – Original Image; 5 – Region of interest; 6 – Segmentation best result.

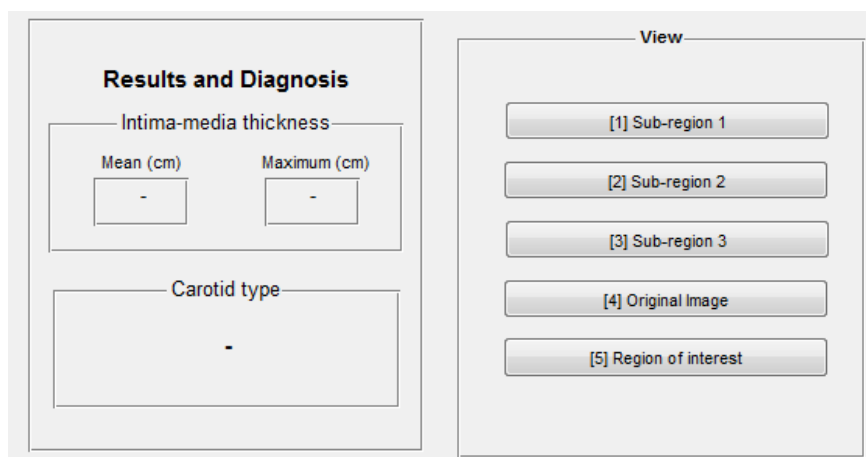


Figure 4.18 – The panel “Results and Diagnosis” present the IMT value and the respective diagnosis. The panel “View” allows to choose which image to display according to the numbering defined.

The method for the selection of the region of interest is chosen in the Segmentation Options. If “Automatic” is selected, the algorithm is implemented in a fully automated way and presents the results as in figure 4.21. On other

hand, if “Semi-automatic” is selected, the algorithm returns two possible regions of interest and the user decides which one contains the far wall of the CCA, as exemplified in figure 4.22.

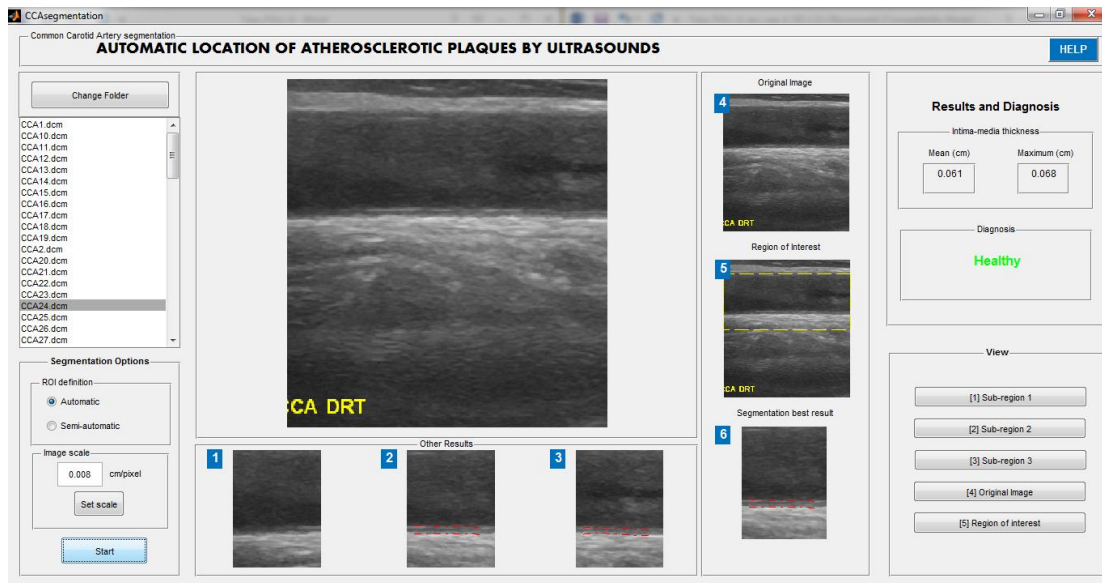


Figure 4.19 - Automatic segmentation of the CCA far wall. On the right, the classification is presented and the values of the mean and maximum thickness are presented.

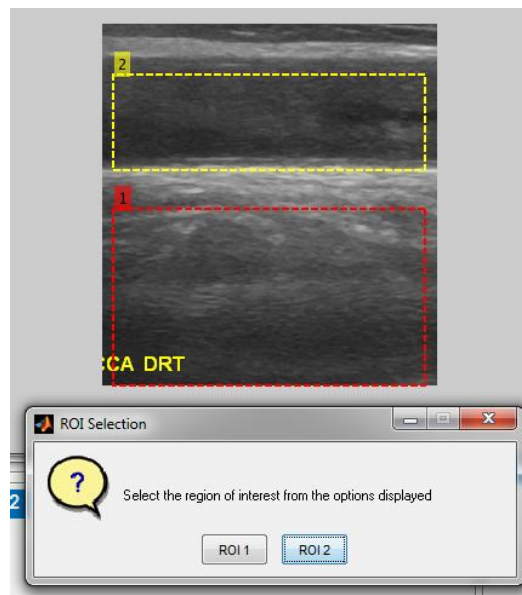


Figure 4.20 - Semi-automatic segmentation of the CCA far wall. Two regions are presented and the user may choose the correct one, containing the far wall of the CCA. On the right, the classification is presented and the values of the mean and maximum thickness are presented.

The described GUI is used to acquire the IMT values for each image, which are crucial to evaluate the performance of the proposed methodology. To use the GUI correctly, three steps should be followed:

1. Select image from the folder chosen;
2. Select between the automatic or semi-automatic method;

3. Set the correct scale according to Appendix C;
4. Push the “Start” button.

5 RESULTS AND DISCUSSION

This chapter presents the results achieved in this thesis. In order to test the performance of the segmentation algorithm, a dataset containing 100 echography of the carotid artery was acquired by an expert, as mentioned in 4.1. The same expert visually analyzed all the images and manually delineated the IMT, being these values compared with the obtained by the algorithm.

5.1 MANUAL MEASUREMENTS

The images were acquired by an expert using a *GE Logiq e Portable Ultrasound System* [46] as referred in 4.1. The same expert visually analyzed all the images and manually delineated the IMT, using ImageJ [51]. Three IMT measurements were carried out for each image and the mean of the values was taken as the “ground-truth” for the respective image.

The figure 5.1 displays the manual measurement of the image “CCA24.dcm”. The scale presented in the right border of the image is used to convert the measurement value from pixels to centimeter. The measurements (labeled as 1, 2 and 3 in the figure) are made along the vessel wall in order to provide a reliable “ground-truth” based on the mean of the three values.

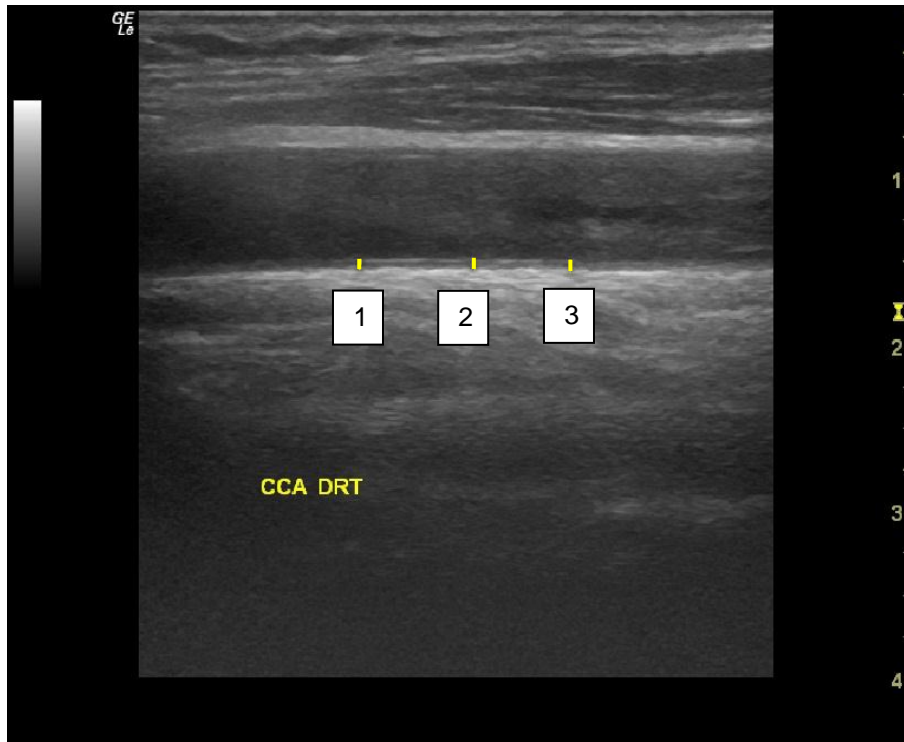


Figure 5.1 – Manual measurement of the image “CCA24.dcm” using ImageJ. 1: 0.061 cm; 2: 0.060 cm; 3: 0.060 cm.

5.2 AUTOMATIC MEASUREMENTS

The automatic segmentation of the IM complex provided the IMT for each one of the images in the dataset. As explained in 4.2.3 the algorithm can provide 3 different IMT values, for each division of the ROI. Furthermore, the algorithm chooses the best result from the computed ones.

The figure 5.2 displays the result of the automatic segmentation for the image “CCA24.dcm”. In this image, the sub-region A does not provide a reliable result and the segmentation is not presented, as referred in 4.2.3. The algorithm also selects the second sub-region as the best result.

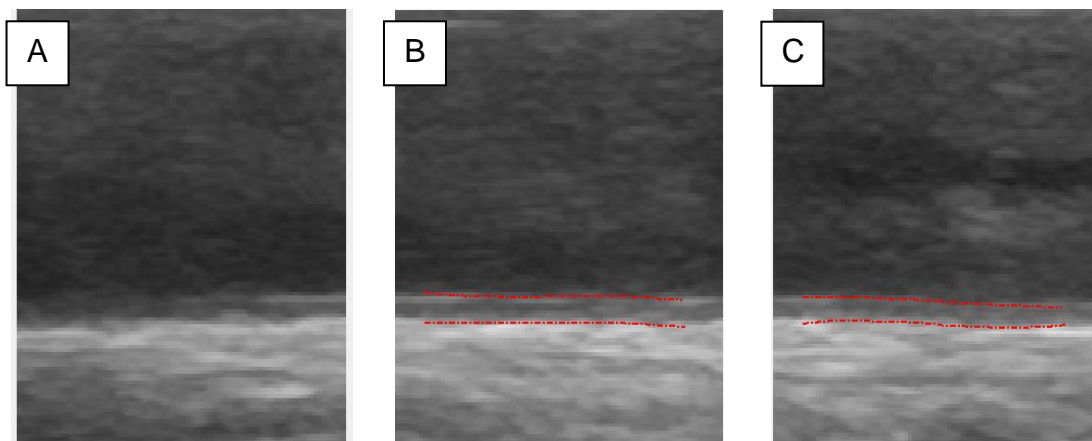


Figure 5.2 – Automatic segmentation of the image “CCA24.dcm”.

For each segmentation result, the maximum and mean value of the IMT in each sub-region is computed. In order to analyze the results of the automatic measurements with the “ground-truth”, the automatic IMT results are grouped in 4 different group. The groups 1 and 2 refer only to the sub-region selected as the best result, while the groups 3 and 4 take into account the results of every sub-region with reliable results. If only one sub-region presents reliable results, the groups 3 and 4 are equal to 1 and 2. The groups are defined as follows:

- Group 1: Mean thickness measured in the sub-region selected as the best result;
- Group 2: Maximum thickness measured in the sub-region selected as the best result;
- Group 3: Average of the individual mean thickness measured in the sub-regions with reliable results;
- Group 4: Mean of the maximum thickness measured in the sub-regions with reliable results.

Additionally, the group 0 was also defined as the “ground-truth” concerning the manual measurements mentioned in 5.1. Those groups are used for the following statistical analysis.

COMPUTATION TIME

The computation time for the segmentation of each image was recorded and the results are presented in Appendix B. On average, the time needed to segment an image was 1.17s. The testing was done on an ASUS N53Jq with a 1.73GHz Intel Core i7 CPU processor and 6GB of memory RAM.

IMAGE SCALE

In the 100 images processed, the scale used to convert pixels to centimeters was not the same in all images, once each image has its own scale. The Appendix C presents the scale values for each image and, on average, the scale was 0.0076 cm per pixel.

5.3 AMBIGUOUS RESULTS

A few images have some artifacts which were not taken into account by the algorithm formulation.

One of the most common disturbances in the results was due to the existence of thyroid nodules which are located near the CCA. These nodules are shown in figure 5.3. On the left side of the figure, the sub-regions of the ROI are depicted with the dashed line and, on the right side (labeled A and B), it is displayed the primary segmentation result. In addition, it is also displayed the full segmentation result, labeled as C.

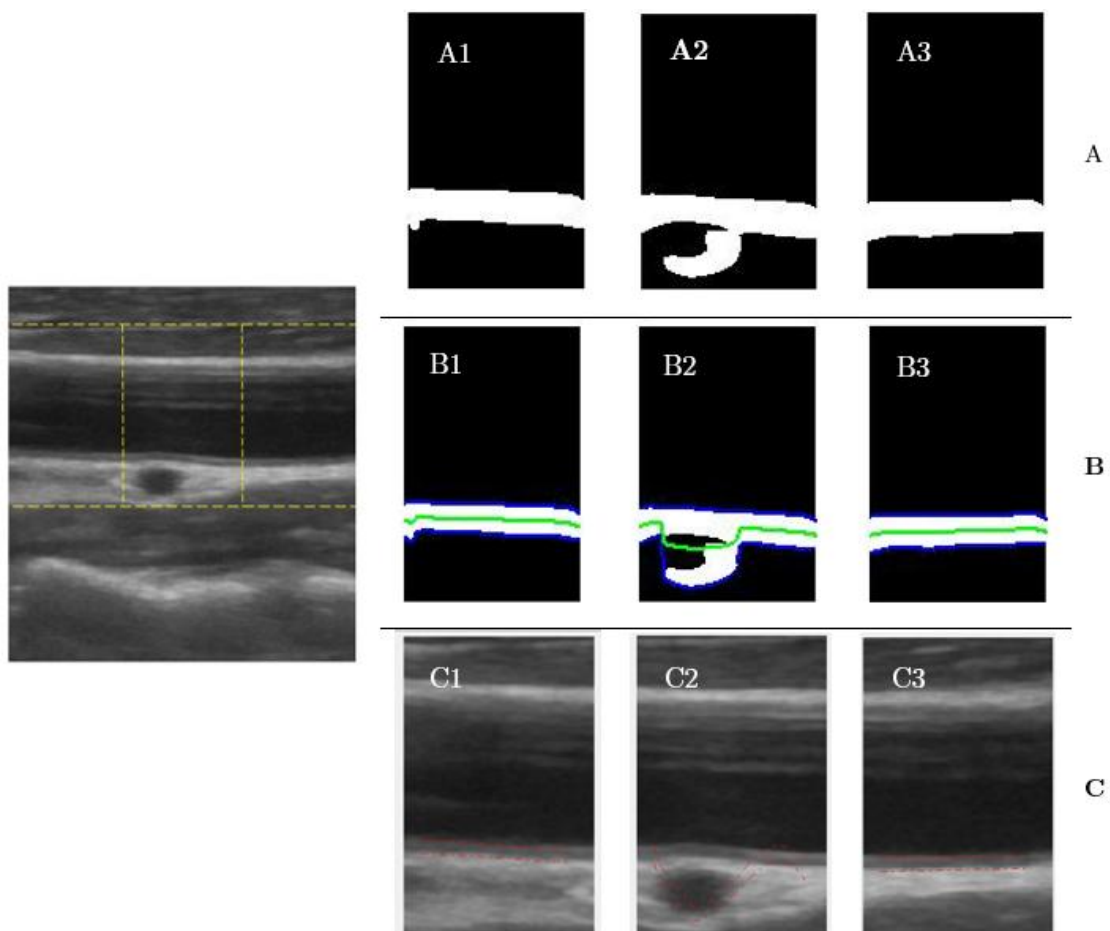


Figure 5.3 – Automatic segmentation failure in an image with thyroid nodules. Image “CCA81.dcm”. Results obtained using MatLab [50].

The image A2 on figure 5.3 shows the sub-region image after thresholding. It is observed that the thyroid nodule was not efficiently separated from the far wall of the carotid artery. For the mentioned reason, the primary segmentation (B2 in figure 5.3) obtained a result that affects the segmentation final result (C1 in figure 5.3), precluding a reliable result. Despite this failure, the

algorithm selected the sub-region C3 as the best result and a similar behaviour was observed in all images with thyroid nodules processed.

5.4 STATISTICAL ANALYSIS

The statistical analysis of the 5 groups (defined in 5.2) aims to find the error between the “ground-truth” measurements (group 0) and the IMT values obtained using the automatic segmentation (groups 1, 2, 3 and 4).

From the 100 echography images, sixteen images were not possible to segment and the IMT was not measured. Eighty-four (84) images were successfully processed, corresponding to 84% of the image dataset. The automatic and manual measurements for the mentioned 84 images are displayed in Appendix A. The results will be studied using 3 distinct analyses presented below.

5.4.1 BLAND-ALTMAN PLOT

A Bland-Altman plot [52] is a method of data plotting used to analyze the agreement between two different assays. One application of the Bland-Altman plot is to compare two clinical measurements which provided some errors in their measure. It can also be used to compare a new measurement technique with a gold standard. Assuming two measurement values, x and y , the Bland-Altman plot [52] is a graph representing each pair (x,y) as follows:

- The abscissa value is the mean of the two measurements: $(x_1+y_1)/2$;
- The ordinate value is the difference between the two measurements: x_1-y_1 ;

As aforementioned, the Bland-Altman plot can be used to compare two clinical measurements that can provide some errors. That is the case in this work, since the measurements made by the expert as well as the ones provided by the algorithm can suffer errors. The Bland-Altman plot also provides the mean error between the measurements as well as the respective standard deviation [52].

Four different Bland-Altman plots were considered, corresponding to the relationships between the group 0 (“ground-truth”) and the groups 1, 2, 3 and 4. The figure 5.4 displays the four Bland-Altman plots and the table 5.1

shows the mean error and respective standard deviation for each relationship. All the images were obtained using GraphPad Prism 6 [53].

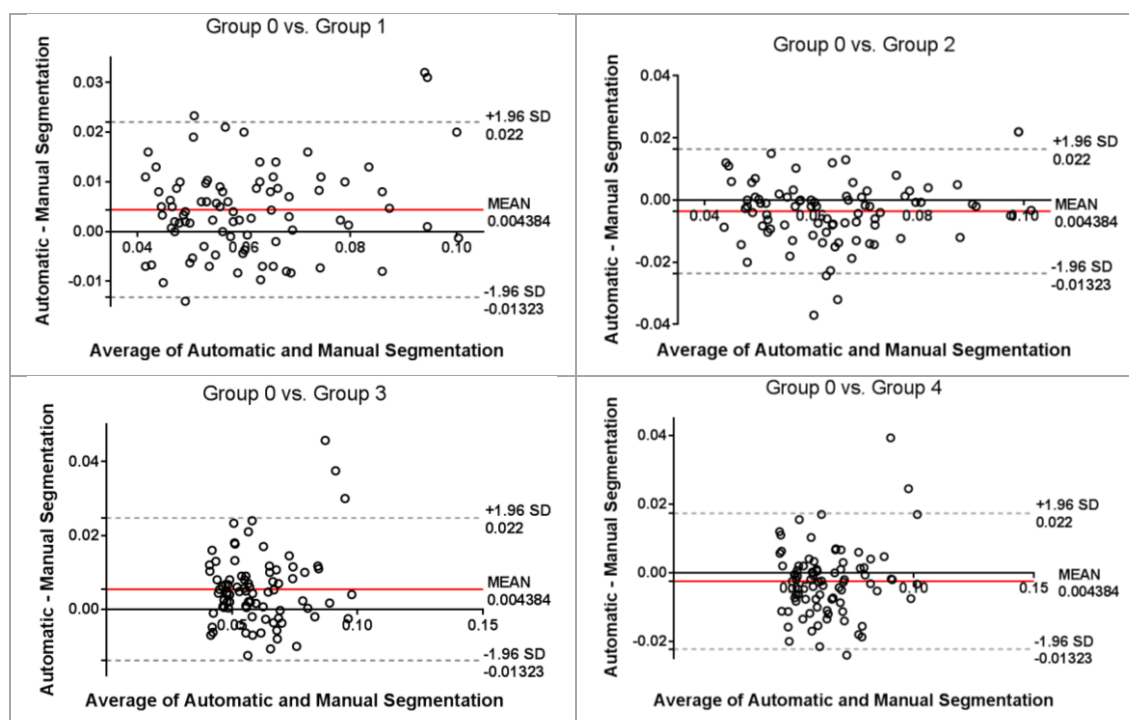


Figure 5.4 – Bland-Altman comparing each of the 4 relationships defined. The mean difference between groups as well as the limits of agreement for a confidence of 95% are shown. Values in centimetres. Graphs obtained using GraphPad Prism 6 [53].

	Group 0 vs. Group 1	Group 0 vs. Group 2	Group 0 vs. Group 3	Group 0 vs. Group 4
Average	0,0044	-0,0036	0,0054	-0,0025
Standard Deviation	0,0090	0,0102	0,0098	0,0101

Table 5.1 - Average and standard deviation of each of the 4 comparisons performed. All values are in centimetres. Data obtained using GraphPad Prism 6 [53].

The Bland-Altman plot enabled a graphical analysis of the measurement error between the algorithm results and the “ground-truth” thickness provided by a specialist. The Bland-Altman plots in figure 5.4 show few outliers in all groups, since almost all data is inside the range defined by the dashed lines.

As shown in table 5.1, the smallest average error (-25 μm) is provided by group 4. However, the standard deviation of this value is the second highest (101 μm), which suggests that the group 4 does not provide reliable data. Group 3, which corresponds to the mean thickness concerning the 3 sub-regions, presents the worst result (54 μm) and suggests that the IMT should not

be measured throughout the entire far wall of the carotid artery, in order to avoid regions which provide erroneous results.

In table 5.1, groups 1 and 2 presented similar absolute error values (44 μm and -36 μm), with the most reliable values, confirming the choice made by the algorithm for the sub-region who has better values. The algorithm formulation define the group 1 as the one with more reliable results (as explained in 5.2) and the average measurement error of this dataset stands at 44 μm with a standard deviation of 90 μm . Since the average value of the scale used was of 76 μm per pixel (see Appendix C), it can be assumed that the algorithm has a good performance in the tested echography images, since the average error is approximately equal to half the value of a pixel. However, the standard deviation of the measurement error precludes the reliability of the algorithm for medical application.

5.4.2 MANN-WHITNEY TEST

The Mann-Whitney test [54] is an unpaired and nonparametric statistical test and it was also applied to each one of the 4 relationships. This test provides a p-value which determines if there is a strong or weak correlation between the data: if the p-value is smaller than 0.05, the groups are not sufficiently similar. The results of the Mann-Whitney test for each different relationship in this work are presented in the table 5.2 and they suggest that groups 1 and 4 have a strong correlation with group 0.

	Group 0 vs. Group 1	Group 0 vs. Group 2	Group 0 vs. Group 3	Group 0 vs. Group 4
P-Value	0,0625	0,0425	0,0190	0,0898

Table 5.2 – P-value of Mann-Whitney test for each relationship. Data obtained using GraphPad Prism 6 [53].

5.4.3 PEARSON'S CORRELATION COEFFICIENT

The Pearson's Correlation coefficient [55] is an indicator of the similarity between groups. This coefficient ranges from -1 to 1 and a high similarity

between groups should result in a Pearson's Correlation Coefficient close to the referred limits. Concerning the performed analysis (table 5.3), the best result was obtained in the correlation between group 0 and group 1, reinforcing the position of the group 1 as the most reliable.

	Group 0 vs. Group 1	Group 0 vs. Group 2	Group 0 vs. Group 3	Group 0 vs. Group 4
Pearson Correlation Coefficient	0,828	0,781	0,793	0,783

Table 5.3 – Pearson's Correlation Coefficient for each relationship. Data obtained using GraphPad Prism 6 [53].

5.5 SUMMARY

The IMT is an important indicator in controlling the atherosclerosis risk and its measurement using ultrasounds is a reliable and non-invasive technique used worldwide. In order to create a standard measure protocol, an automatic segmentation algorithm with consistent and reliable results can be a core feature to make this task less human dependent, providing a fast diagnostic.

According to the discussed results, group 1 proved to be the group with more reliable results, due to its performance in the Mann-Whitney U Test and in the Pearson's Correlation Coefficient. As seen in Appendix B, the time needed to process a single image with the algorithm was 1.17 seconds. This computational performance allows a fast diagnosis after the image acquisition.

Regarding the measurement error (44 μm), the result of the group 1 is not excellent but it demonstrates to have the smaller standard deviation (90 μm), which suggest a more reliable result. In addition, the algorithm was able to segment 84% of 100 carotid images, automatically detecting the ROI in each image, one of the most difficult tasks in the medical imaging techniques and segmentation algorithms. The measurement error obtained is similar to the work of Gutierrez et al. [36] and Delsanto et al. [39] while Liguori et al. [27], Faita et al. [29] and Molinari et al. [42] obtained a better result, which suggests that the algorithm should be improved to be used in medical application.

6 CONCLUSIONS AND FUTURE WORK

6.1 CONCLUSIONS

This work proposes an automatic detection algorithm of the atheromatous plaque by ultrasound images, a technique used worldwide but still with no reliable full automation and that requires the supervision of a specialist. In order to do so, the steps followed were:

- Studying the problem, reviewing about the cardiovascular diseases, namely the atherosclerosis, as well as the segmentation techniques already implemented in order to fill this gap;
- Gathering ultrasound images of the CCA in order to create a dataset to work on;
- Developing the algorithm, taking into account the need of full automation and minor human interaction;
- Evaluation the performance of the algorithm on the gathered dataset.

The automatic recognition of the ROI was implemented in a simple and fast step, using thresholding. Then, the segmentation was achieved using the first-order derivative of the Gaussian function as an edge detector, creating two well-defined intensity peaks in the vertical intensity gradient of the image. These two peaks correspond to the intima-media and lumen-intima interfaces, respectively. In addition to the information derived from each image, a-priori knowledge about the maximum and minimum IMT was used to select the

acceptable points from the obtained set. This step allowed the elimination of outliers, thus obtaining an improved result for each segmentation.

Using the described automated algorithm it was possible to identify the correct ROI, containing the far wall of the CCA, and measure the thickness of the intima-media complex in a considerable amount of images (84%) in a reduced time, a noteworthy result considering the complexity of the task even for an expert. After testing the algorithm results with Bland-Altman plots, Mann-Whitney U Tests and Pearson Correlations, they proved reliable and with an average error of 44 μm , with a standard deviation of 90 μm .

Taking the results mentioned before into account, the performance of the implement algorithm is comparable to that of Gutierrez et al. [36] and Delsanto et al. [39]. However, the standard deviation of the error obtained (90 μm) can preclude a medical application before some improvements in the algorithm are made, since an error of this magnitude can provide an erroneous diagnosis: the IMT difference between a healthy (~ 0.06 cm) and an unhealthy (~ 0.09 cm) carotid [48] is approximately three times the standard deviation. The used dataset contained images with very different characteristics and the goal was to reject the smallest amount so the algorithm could be able to segment images with different appearances. This lowered the quality of the global IMT measurement, providing an error with a substantial standard deviation, but demonstrating the versatility of the proposed algorithm.

In conclusion, computed algorithms for the processing of carotid ultrasound images have continuously grown in number and performance in the latter years. However, the full automation of the process is still a big issue in this type of approaches. The algorithm proposed in this thesis has an acceptable behavior on this task, once it is able to automatically identify the region of interest. Possible improvements in the approach are discussed in the next section.

6.2 FUTURE WORK

The potential benefits coming from the use of the computer-aided segmentation techniques are the reduction of the examination time, the increased accuracy in the IMT measurement and the reduction of the

subjectivity. In spite of the promising results, future work is necessary before this approach is suitable for clinical use. The analysis is performed on a limited number of examples (100 images), and this it would be beneficial to determine the efficacy of the algorithm on more datasets.

Since 16% of the dataset was not able to provide results mostly due to speckle noise, it would be important to improve the image despeckling in order to enhance the structures in the wall of the carotid artery (lumen-intima and media-adventitia interfaces). The ROI selection proved to have reliable results in all images of the dataset, which suggests that, with an improvement in the IMT measurement can allow the medical application.

In conclusion, despite the many improvements which can be devised to the proposed algorithm, it represents a viable approach for the IMT measurement. The performance varies due to considerable variability in the scale, resolution and discernibility of the acquired data. However, the successful segmentation results abide strong visual and quantitative correspondence to the location of the far wall of the carotid artery.

7 REFERENCES

- [1] S. Yusuf, S. Ounpuu, and S. Anand, "The global epidemic of atherosclerotic cardiovascular disease," *Med. Princ. Pract.*, vol. 11 Suppl 2, pp. 3–8, 2002.
- [2] D. H. O’Leary and M. L. Bots, "Imaging of atherosclerosis: carotid intima-media thickness," *Eur. Heart J.*, 2010.
- [3] I. Solovey, "Segmentation of 3D Carotid Ultrasound Images Using Weak Geometric Priors," University of Waterloo, 2010.
- [4] R. C. Pasternak, M. H. Criqui, E. J. Benjamin, F. G. R. Fowkes, E. M. Isselbacher, P. A. McCullough, P. A. Wolf, and Z.-J. Zheng, "Atherosclerotic Vascular Disease Conference: Writing Group I: epidemiology," *Circulation*, vol. 109, no. 21, pp. 2605–2612, 2004.
- [5] W. J. Insull, "The pathology of atherosclerosis: plaque development and plaque responses to medical treatment," *Am. J. Med.*, vol. 122, no. 1 Suppl, pp. S3–S14, 2009.
- [6] D. Mozaffarian, E. J. Benjamin, and et al, "Heart disease and stroke statistics--2015 update: a report from the American Heart Association," *Circulation*, vol. 131, no. 4, pp. 29–322, 2015.
- [7] J. Pereira, "Multi Scale Lumen Boundaries Segmentation and its 3D Representation," University of Porto, 2012.
- [8] A. J. Lusis, "Genetics of atherosclerosis," *Trends Genet.*, vol. 28, no. 6, pp. 267–275, 2012.
- [9] H. Ashrafian, "Anatomically specific clinical examination of the carotid arterial tree," *Anat. Sci. Int.*, vol. 82, no. 1, pp. 16–23, 2007.
- [10] A. J. Lusis and et al, "Genetics of atherosclerosis," *Annu. Rev. Genomics Hum. Genet.*, vol. 5, pp. 189–218, 2004.
- [11] A. Eriksson and P. Mattsson, "Segmentation of Carotid Arteries from 3D and 4D Ultrasound Images," Linköping University, 2002.
- [12] R. Klooster, "Automated Image Segmentation and Registration of Vessel Wall MRI for Quantitative Assessment of Carotid Artery Vessel Wall

- Dimensions and Plaque Composition,” University of Leiden, 2014.
- [13] C. Guy and D. Ffytche, *Introduction to the Principles of Medical Imaging*. London: Imperial College Press, 2005.
- [14] K. K. Shung, M. Smith, and B. M. W. Tsui, *Principles of Medical Imaging*. Cambridge: Academic Press, 1992.
- [15] J. A. Jensen, *Estimation of Blood Velocities Using Ultrasound - A Signal Processing Approach*. Cambridge University Press, 1996.
- [16] O. V. Michailovich and A. Tannenbaum, “Despeckling of medical ultrasound images,” *IEEE Trans. Ultrason. Ferroelectr. Freq. Control*, vol. 53, no. 1, pp. 64–78, 2006.
- [17] C. P. Loizou, C. S. Pattichis, C. I. Christodoulou, R. S. H. Istepanian, M. Pantziaris, and A. Nicolaides, “Comparative evaluation of despeckle filtering in ultrasound imaging of the carotid artery,” *IEEE Trans. Ultrason. Ferroelectr. Freq. Control*, vol. 52, no. 10, pp. 1653–1669, 2005.
- [18] J. R. 3rd Crouse, “Thematic review series: patient-oriented research. Imaging atherosclerosis: state of the art,” *J. Lipid Res.*, vol. 47, no. 8, pp. 1677–1699, 2006.
- [19] P.-J. Touboul, M. G. Hennerici, and et al, “Mannheim carotid intima-media thickness and plaque consensus (2004-2006-2011). An update on behalf of the advisory board of the 3rd, 4th and 5th watching the risk symposia, at the 13th, 15th and 20th European Stroke Conferences,” *Cerebrovasc. Dis.*, vol. 34, no. 4, pp. 290–296, 2012.
- [20] M. Gaarder and T. Seierstad, “Measurements of carotid intima media thickness in non-invasive high-frequency ultrasound images: the effect of dynamic range setting,” *Cardiovasc. Ultrasound*, vol. 13, no. 1, pp. 1–5, 2015.
- [21] P. Pignoli, E. Tremoli, A. Poli, P. Oreste, and R. Paoletti, “Intimal plus medial thickness of the arterial wall: a direct measurement with ultrasound imaging,” *Circulation*, vol. 74, no. 6, pp. 1399–1406, 1986.
- [22] I. B. Casella, C. Presti, R. M. P. Porta, C. R. D. Sabbag, M. A. Bosch, and Y. Yamazaki, “A practical protocol to measure common carotid artery intima-media thickness,” *Clinics (Sao Paulo)*, vol. 63, no. 4, pp. 515–520, 2008.
- [23] G. Rodriguez-Granillo and P. Serruys, “Assessment of carotid plaque with intravascular ultrasound,” in *Carotid Disease*, Cambridge University Press, 2006, p. 223,224.
- [24] P. J. Touboul, P. Prati, P. Y. Scarabin, V. Adrai, E. Thibout, and P. Ducimetiere, “Use of monitoring software to improve the measurement of carotid wall thickness by B-mode imaging,” *J. Hypertens.* 10, vol. 5, pp. S37–41, 1992.
- [25] P. Pignoli and T. Longo, “Evaluation of atherosclerosis with B-mode ultrasound imaging,” *J. Nucl. Med. Allied Sci.* 32, vol. 3, pp. 166–173, 1988.
- [26] F. Molinari, G. Zeng, and J. S. Suri, “A state of the art review on intima-

- media thickness (IMT) measurement and wall segmentation techniques for carotid ultrasound,” *Comput. Methods Programs Biomed.*, vol. 100, no. 3, pp. 201–221, 2010.
- [27] C. Liguori, A. Paolillo, and A. Pietrosanto, “An automatic measurement system for the evaluation of carotid intima-media thickness,” *Instrumentation and Measurement, IEEE Transactions on*, vol. 50, no. 6, pp. 1684–1691, 2001.
- [28] J. H. Stein, C. E. Korcarz, M. E. Mays, P. S. Douglas, M. Palta, H. Zhang, T. Lecaire, D. Paine, D. Gustafson, and L. Fan, “A semiautomated ultrasound border detection program that facilitates clinical measurement of ultrasound carotid intima-media thickness,” *J. Am. Soc. Echocardiogr.*, vol. 18, no. 3, pp. 244–251, 2005.
- [29] F. Faita, V. Gemignani, E. Bianchini, C. Giannarelli, L. Ghiadoni, and M. Demi, “Real-time measurement system for evaluation of the carotid intima-media thickness with a robust edge operator,” *J. Ultrasound Med.*, vol. 27, no. 9, pp. 1353–1361, 2008.
- [30] C. Schmidt and I. Wendelhag, “How can the variability in ultrasound measurement of intima-media thickness be reduced? Studies of interobserver variability in carotid and femoral arteries,” *Clin. Physiol.*, vol. 19, no. 1, pp. 45–55, 1999.
- [31] I. Wendelhag, O. Wiklund, and J. Wikstrand, “Arterial wall thickness in familial hypercholesterolemia. Ultrasound measurement of intima-media thickness in the common carotid artery,” *Arterioscler. Thromb.*, vol. 12, no. 1, pp. 70–77, 1992.
- [32] Q. Liang, I. Wendelhag, J. Wikstrand, and T. Gustavsson, “A multiscale dynamic programming procedure for boundary detection in ultrasonic artery images,” *IEEE Trans. Med. Imaging*, vol. 19, no. 2, pp. 127–142, 2000.
- [33] I. Wendelhag, O. Wiklund, and J. Wikstrand, “On Quantifying Plaque Size and Intima-Media Thickness in Carotid and Femoral Arteries: Comments on Results From a Prospective Ultrasound Study in Patients With Familial Hypercholesterolemia,” *Arterioscler. Thromb. Vasc. Biol.*, vol. 16, pp. 843–850, 1996.
- [34] I. Wendelhag, Q. Liang, T. Gustavsson, and J. Wikstrand, “A new automated computerized analyzing system simplifies readings and reduces the variability in ultrasound measurement of intima-media thickness,” *Stroke.*, vol. 28, no. 11, pp. 2195–200, 1997.
- [35] D. J. Williams and M. Shah, “A Fast algorithm for active contours and curvature estimation,” *CVGIP: Image Understanding*, vol. 55, no. 1, pp. 14–26, 1992.
- [36] M. A. Gutierrez, P. E. Pilon, S. G. Lage, L. Kopel, R. T. Carvalho, and S. S. Furuie, “Automatic measurement of carotid diameter and wall thickness in ultrasound images,” *Computers in Cardiology, 2002.* pp. 359–362, 2002.
- [37] D. Cheng, A. Schmidt-Trucksass, K. Cheng, and H. Burkhardt, “Using

- snakes to detect the intimal and adventitial layers of the common carotid artery wall in sonographic images,” *Comput. Methods Programs Biomed.*, vol. 67, no. 1, pp. 27–37, 2002.
- [38] C. P. Loizou, C. S. Pattichis, M. Pantziaris, T. Tyllis, and A. Nicolaides, “Snakes based segmentation of the common carotid artery intima media,” *Med. Biol. Eng. Comput.*, vol. 45, no. 1, pp. 35–49, 2007.
- [39] S. Delsanto, F. Molinari, P. Giustetto, W. Liboni, and S. Badalamenti, “CULEX-completely user-independent layers extraction: ultrasonic carotid artery images segmentation,” *Conf. Proc. ... Annu. Int. Conf. IEEE Eng. Med. Biol. Soc. IEEE Eng. Med. Biol. Soc. Annu. Conf.*, vol. 6, pp. 6468–6471, 2005.
- [40] S. Delsanto, F. Molinari, P. Giustetto, W. Liboni, S. Badalamenti, and J. S. Suri, “Characterization of a Completely User-Independent Algorithm for Carotid Artery Segmentation in 2-D Ultrasound Images,” *Instrumentation and Measurement, IEEE Transactions on*, vol. 56, no. 4, pp. 1265–1274, 2007.
- [41] S. Delsanto, F. Molinari, W. Liboni, P. Giustetto, S. Badalamenti, and J. S. Suri, “User-independent plaque characterization and accurate IMT measurement of carotid artery wall using ultrasound,” *Conf. Proc. ... Annu. Int. Conf. IEEE Eng. Med. Biol. Soc. IEEE Eng. Med. Biol. Soc. Annu. Conf.*, vol. 1, pp. 2404–2407, 2006.
- [42] F. Molinari, G. Zeng, and J. S. Suri, “An integrated approach to computer-based automated tracing and its validation for 200 common carotid arterial wall ultrasound images: a new technique,” *J. Ultrasound Med.*, vol. 29, no. 3, pp. 399–418, 2010.
- [43] F. Destrempes, J. Meunier, M. F. Giroux, G. Soulez, and G. Cloutier, “Segmentation in Ultrasonic B-Mode Images of Healthy Carotid Arteries Using Mixtures of Nakagami Distributions and Stochastic Optimization,” *Medical Imaging, IEEE Transactions on*, vol. 28, no. 2, pp. 215–229, 2009.
- [44] S. Golemati, J. Stoitsis, T. Balkizas, and K. S. Nikita, “Comparison of B-mode, M-mode and Hough transform methods for measurement of arterial diastolic and systolic diameters,” *Engineering in Medicine and Biology Society, 2005. IEEE-EMBS 2005. 27th Annual International Conference of the*, pp. 1758–1761, 2005.
- [45] S. Golemati, J. Stoitsis, E. G. Sifakis, T. Balkizas, and K. S. Nikita, “Using the Hough transform to segment ultrasound images of longitudinal and transverse sections of the carotid artery,” *Ultrasound Med. Biol.*, vol. 33, no. 12, pp. 1918–1932, 2007.
- [46] *LOGIQ e User Guide*. Milwaukee: General Electric Co., 2010.
- [47] “Health informatics -- Digital imaging and communication in medicine (DICOM) including workflow and data management,” ISO 12052, 2006.
- [48] A. C. S. Nogueira, C. D. Schettino, M. V. L. Barros, M. L. de Alcantara, P. C. de C. Studart, P. P. de Araújo, S. I. do Amaral, and S. Barretto, “Normatização dos equipamentos e das técnicas para a realização de

- exames de ultra-sonografia vascular ,” *Arquivos Brasileiros de Cardiologia* , vol. 82 . scielo , pp. 1–14, 2004.
- [49] M. C. Bastida-Jumilla, R. M. Menchón-Lara, J. Morales-Sánchez, R. Verdú-Monedero, J. Larrey-Ruiz, and J. L. Sancho-Gómez, “Segmentation of the common carotid artery walls based on a frequency implementation of active contours: Segmentation of the common carotid artery walls,” *J. Digit. Imaging*, vol. 26, no. 1, pp. 129–139, 2013.
- [50] “MATLAB.” The MathWorks, Inc, 2014.
- [51] W. Rasband, “ImageJ.” National Institutes of Health, USA, Maryland.
- [52] J. M. Bland and D. G. Altman, “Statistical methods for assessing agreement between two methods of clinical measurement,” *Lancet*, 1986.
- [53] “GraphPad Prism 6.” GraphPad Software, Inc, 2015.
- [54] H. B. Mann and D. R. Whitney, “On a test of wheter one of two random variables is stochastically larger than the other,” *Ann. Math. Stat.*, vol. 18, pp. 50–60, 1947.
- [55] K. Pearson, “Not on Regression and Inheritance in the Case of Two Parents,” *Proc R Soc*, vol. 58, pp. 240–242, 1895.

APPENDIX A

This appendix displays the IMT values for each group defined in 5.2.

	Group 0	Group 1	Group 2	Group 3	Group 4
CCA1	0,0600	0,0670	0,0680	0,0707	0,0840
CCA2	0,0690	0,0610	0,0750	0,0693	0,0877
CCA3	0,0627	0,0600	0,0700	0,0620	0,0700
CCA4	0,0547	0,0630	0,0660	0,0617	0,0647
CCA5	0,0523	0,0570	0,0750	0,0587	0,0677
CCA6	0,0680	0,0580	0,0760	0,0717	0,0860
CCA7	0,0467	0,0530	0,0570	0,0423	0,0540
CCA8	0,0477	0,0530	0,0570	0,0423	0,0540
CCA9	0,0393	0,0460	0,0480	0,0455	0,0505
CCA10	0,0530	0,0430	0,0460	0,0450	0,0510
CCA11	0,0590	0,0570	0,0610	0,0510	0,0617
CCA12	0,0623	0,0390	0,0520	0,0390	0,0520
CCA13	0,0517	0,0430	0,0460	0,0450	0,0510
CCA14	0,0577	0,0480	0,0680	0,0445	0,0575
CCA15	0,0783	0,0700	0,0770	0,0700	0,0770
CCA16	0,0670	0,0460	0,0670	0,0460	0,0670
CCA17	0,0720	0,0650	0,0690	0,0650	0,0690
CCA18	0,0420	0,0560	0,0790	0,0430	0,0533
CCA19	0,0503	0,0470	0,0500	0,0457	0,0507
CCA20	0,0673	0,0630	0,0660	0,0697	0,0723
CCA21	0,0583	0,0680	0,0770	0,0647	0,0703
CCA22	0,0650	0,0670	0,0720	0,0707	0,0737
CCA23	0,0493	0,0430	0,0540	0,0430	0,0540
CCA24	0,0603	0,0610	0,0680	0,0560	0,0640
CCA25	0,0647	0,0730	0,0790	0,0683	0,0760
CCA26	0,0803	0,0790	0,0810	0,0800	0,0835
CCA27	0,0693	0,0690	0,0710	0,0640	0,0720
CCA28	0,0603	0,0580	0,0610	0,0587	0,0627
CCA29	0,0553	0,0530	0,0690	0,0505	0,0630
CCA30	0,0640	0,0720	0,0780	0,0720	0,0780
CCA31	0,0380	0,0450	0,0580	0,0450	0,0580
CCA32	0,0397	0,0500	0,0540	0,0445	0,0555
CCA33	0,0463	0,0430	0,0490	0,0360	0,0443
CCA34	0,0487	0,0470	0,0550	0,0483	0,0550
CCA35	0,0700	0,0670	0,0720	0,0625	0,0720

CCA36	0,0900	0,0770	0,0850	0,0790	0,0853
CCA37	0,1100	0,0780	0,0880	0,0725	0,0855
CCA38	0,1100	0,0900	0,1060	0,0800	0,0930
CCA39	0,1100	0,0790	0,0880	0,0643	0,0707
CCA40	0,0900	0,0820	0,0920	0,0783	0,0920
CCA41	0,0600	0,0540	0,0600	0,0540	0,0595
CCA42	0,0700	0,0500	0,0580	0,0460	0,0530
CCA43	0,0600	0,0410	0,0450	0,0420	0,0445
CCA44	0,0500	0,0370	0,0390	0,0370	0,0390
CCA45	0,0500	0,0340	0,0380	0,0340	0,0380
CCA46	0,0600	0,0520	0,0660	0,0510	0,0590
CCA47	0,0600	0,0560	0,0600	0,0423	0,0567
CCA48	0,0500	0,0480	0,0510	0,0460	0,0520
CCA49	0,0700	0,0560	0,0690	0,0600	0,0690
CCA50	0,0800	0,0640	0,0720	0,0655	0,0740
CCA51	0,0800	0,0690	0,0770	0,0685	0,0785
CCA52	0,0576	0,0620	0,0650	0,0555	0,0640
CCA53	0,0620	0,0690	0,0750	0,0647	0,0697
CCA54	0,0707	0,0620	0,0650	0,0590	0,0640
CCA55	0,0793	0,0770	0,0800	0,0770	0,0800
CCA56	0,0840	0,0740	0,0800	0,0740	0,0800
CCA57	0,0707	0,0780	0,0830	0,0807	0,0863
CCA58	0,0583	0,0620	0,0720	0,0563	0,0693
CCA59	0,0820	0,0900	0,0940	0,0840	0,0873
CCA60	0,0897	0,0850	0,0910	0,0880	0,0915
CCA61	0,0570	0,0580	0,0720	0,0590	0,0705
CCA62	0,0667	0,0580	0,0710	0,0620	0,0710
CCA63	0,0470	0,0420	0,0650	0,0460	0,0605
CCA64	0,0467	0,0460	0,0550	0,0460	0,0550
CCA65	0,0500	0,0480	0,0490	0,0480	0,0505
CCA66	0,0510	0,0470	0,0520	0,0470	0,0520
CCA67	0,0470	0,0470	0,0510	0,0465	0,0515
CCA68	0,0510	0,0540	0,0590	0,0553	0,0587
CCA69	0,0500	0,0570	0,0630	0,0625	0,0715
CCA70	0,0490	0,0440	0,0810	0,0470	0,0660
CCA71	0,0560	0,0500	0,0550	0,0550	0,0600
CCA72	0,0480	0,0400	0,0420	0,0400	0,0417
CCA73	0,0580	0,0530	0,0580	0,0530	0,0580
CCA74	0,0560	0,0560	0,0580	0,0555	0,0580
CCA75	0,0730	0,0590	0,0600	0,0623	0,0663
CCA76	0,0950	0,0940	0,1000	0,0975	0,1025
CCA77	0,0997	0,1010	0,1030	0,0957	0,1030
CCA78	0,0710	0,0600	0,0750	0,0540	0,0640

CCA79	0,0507	0,0490	0,0750	0,0440	0,0625
CCA80	0,0550	0,0490	0,0530	0,0490	0,0530
CCA81	0,0577	0,0520	0,0580	0,0520	0,0585
CCA82	0,0470	0,0360	0,0490	0,0350	0,0413
CCA83	0,0583	0,0480	0,0550	0,0493	0,0543
CCA84	0,0600	0,0510	0,0620	0,0530	0,0590

Table 1 – Manual (group 0) and automatic measurements (groups 1, 2, 3 and 4) of 84 images of the carotid artery. All values presented are in cm.

APPENDIX B

This appendix displays the time-consumption to process each image of the dataset using the proposed algorithm.

Image	Elapsed time						
CCA1	1,3000	CCA22	1,2200	CCA43	1,3100	CCA63	1,0000
CCA2	1,1900	CCA23	1,1400	CCA44	1,1700	CCA64	1,1200
CCA3	1,6700	CCA24	1,1600	CCA45	1,2300	CCA65	1,0900
CCA4	1,3300	CCA25	1,1500	CCA46	1,1400	CCA66	1,0900
CCA5	1,2100	CCA26	1,1600	CCA47	1,2600	CCA67	1,3100
CCA6	1,5500	CCA27	1,1000	CCA48	1,2200	CCA68	1,1000
CCA7	1,4100	CCA28	1,1800	CCA49	1,1000	CCA69	1,1200
CCA8	1,5000	CCA29	1,0000	CCA50	1,2800	CCA70	1,2200
CCA9	1,5100	CCA30	1,1600	CCA51	1,2700	CCA71	1,0200
CCA10	1,1300	CCA31	1,0700	CCA52	1,1700	CCA72	0,9000
CCA11	1,1300	CCA32	1,1300	CCA53	1,1300	CCA73	1,0200
CCA12	1,0400	CCA33	1,1000	CCA54	1,1000	CCA74	1,1400
CCA13	1,1600	CCA34	1,1000	CCA55	1,1700	CCA75	1,1500
CCA14	1,1100	CCA35	1,4300	CCA56	1,0900	CCA76	1,1400
CCA15	1,0100	CCA36	1,2100	CCA57	1,0900	CCA77	1,0000
CCA16	1,1500	CCA37	1,4800	CCA58	1,0400	CCA78	1,0200
CCA17	1,2300	CCA38	1,6000	CCA59	1,0500	CCA79	1,1500
CCA18	1,3200	CCA39	1,2000	CCA60	1,0500	CCA80	1,0800
CCA19	1,3400	CCA40	1,1500	CCA61	1,1300	CCA81	1,1500
CCA20	1,1100	CCA41	1,1200	CCA62	1,1200	CCA82	1,1100
CCA21	1,1100	CCA42	1,1800	CCA43	1,1200	CCA83	1,2300

Table 1 – Computation time in seconds for each image processed.

APPENDIX C

This appendix displays the scale values for each image in the dataset used.

Image	Scale	Image	Scale	Image	Scale	Image	Scale
CCA1	0,0070	CCA22	0,0080	CCA43	0,0065	CCA63	0,0080
CCA2	0,0070	CCA23	0,0080	CCA44	0,0051	CCA64	0,0080
CCA3	0,0070	CCA24	0,0080	CCA45	0,0057	CCA65	0,0080
CCA4	0,0070	CCA25	0,0080	CCA46	0,0046	CCA66	0,0080
CCA5	0,0070	CCA26	0,0080	CCA47	0,0051	CCA67	0,0080
CCA6	0,0070	CCA27	0,0080	CCA48	0,0057	CCA68	0,0080
CCA7	0,0080	CCA28	0,0080	CCA49	0,0057	CCA69	0,0080
CCA8	0,0080	CCA29	0,0080	CCA50	0,0057	CCA70	0,0080
CCA9	0,0080	CCA30	0,0090	CCA51	0,0057	CCA71	0,0080
CCA10	0,0080	CCA31	0,0080	CCA52	0,0057	CCA72	0,0080
CCA11	0,0080	CCA32	0,0080	CCA53	0,0080	CCA73	0,0090
CCA12	0,0080	CCA33	0,0080	CCA54	0,0080	CCA74	0,0090
CCA13	0,0080	CCA34	0,0080	CCA55	0,0080	CCA75	0,0080
CCA14	0,0080	CCA35	0,0080	CCA56	0,0080	CCA76	0,0080
CCA15	0,0080	CCA36	0,0063	CCA57	0,0080	CCA77	0,0080
CCA16	0,0080	CCA37	0,0063	CCA58	0,0080	CCA78	0,0080
CCA17	0,0080	CCA38	0,0057	CCA59	0,0090	CCA79	0,0080
CCA18	0,0080	CCA39	0,0057	CCA60	0,0090	CCA80	0,0080
CCA19	0,0080	CCA40	0,0057	CCA61	0,0090	CCA81	0,0080
CCA20	0,0080	CCA41	0,0057	CCA62	0,0090	CCA82	0,0080
CCA21	0,0080	CCA42	0,0065	CCA43	0,0080	CCA83	0,0080

Table 1 – Scale used in each image. All values are in cm/pixel.